Atomic-scale structure of disordered $Ga_{1-x}In_xP$ alloys

A. Silverman
Physics Department, Technion–Israel Institute of Technology, 32000 Haifa, Israel
and Solid State Institute, Technion–Israel Institute of Technology, 32000 Haifa, Israel

Alex Zunger
National Renewable Energy Laboratory, Golden, Colorado 80401

R. Kalish
Physics Department, Technion–Israel Institute of Technology, 32000 Haifa, Israel
and Solid State Institute, Technion–Israel Institute of Technology, 32000 Haifa, Israel

Joan Adler
Physics Department, Technion–Israel Institute of Technology, 32000 Haifa, Israel
(Received 15 September 1994)

Extended x-ray-absorption fine-structure experiments have previously demonstrated that for each composition x, the sample average of all nearest-neighbor A-C distances in an $A_{1-x}B_xC$ semiconductor alloy is closer to the values in the *pure* ($x \to 0$) AC compound than to the composition-weighted (virtual) lattice average. Such experiments do not reveal, however, the distribution of atomic positions in an alloy, so the principle displacement directions and the degrees of correlation among such atomic displacements remain unknown. Here we calculate both structural and thermodynamic properties of $Ga_{1-x}In_xP$ alloys using an *explicit* occupation- *and* position-dependent energy functional. The latter is taken as a modified valence force field, carefully fit to structural energies determined by first-principles local-density calculations. Configurational and vibrational degrees of freedom are then treated via the continuous-space Monte Carlo approach. We find good agreement between the calculated and measured mixing enthalpy of the random alloy, nearest-neighbor bond lengths, and temperature-composition phase diagram. In addition, we predict yet unmeasured quantities such as (a) distributions, fluctuations, and moments of first- and second-neighbor bond lengths as well as bond angles, (b) radial distribution functions, (c) the dependence of short-range order on temperature, and (d) the effect of temperature on atomic displacements. Our calculations provide a detailed picture of how atoms are arranged in substitutionally random but positionally relaxed alloys, and offer an explanation for the effects of site correlations, static atomic relaxations, and dynamic vibrations on the phase-diagram and displacement maps. We find that even in a chemically random alloy (where sites are occupied by Ga or In according to a coin toss), there exists a highly correlated static position distribution whereby the P atoms are displaced deterministically in certain high-symmetry directions.

I. INTRODUCTION

Solid solutions $A_{1-x}B_xC$ between the semiconductor binary constituents AC and BC are often used to attain physical properties $P(x)$ that are intermediate between the end points P_{AC} and P_{BC}.[1,2] Phenomenologically, this is often described by a quadratic form

$$P(A_{1-x}B_xC)=[(1-x)P_{AC}+xP_{BC}]+bx(1-x)\,, \quad (1.1)$$

where b is the bowing coefficient. This description holds for band gaps, elastic constants, carrier mobilities, excess enthalpies, etc.[3] It is now known[4,5] that b [hence $P(x)$] is strongly influenced by the atomic structure of the alloy, i.e., by the extent to which atoms are displaced from the ideal sites of a virtual alloy. For example, calculations[4,5] show that for P=band gap, the optical bowing b is strongly affected by atomic displacements off the ideal sites. Likewise, for P=mixing enthalpy, the interaction parameter b was predicted[6] to be highly sensitive to the size-mismatch-induced atomic relaxation. An extreme example of the dependence of b on atomic structure is the occurrence of widely different band gaps and formation enthalpies found in ordered versus disordered $Ga_{0.5}In_{0.5}P$ alloys of the same composition.[7] Structural relaxation also plays a critical role in determining the pattern of x-ray diffuse scattering in alloys[8] as well as in the exciton dynamics[9] and the phonon spectra.[10] However, understanding the nature of the structure in disordered alloys on an atomic scale is complicated by the fact that there are numerous local atomic environments, so only some average structure is measurable. This can be illustrated by considering an alloy formed from the fourfold-coordinated constituents GaP and InP. While in the pure compounds, phosphorous is coordinated just by Ga_4 (in GaP) or by In_4 (in InP), in the $Ga_{1-x}In_xP$ alloy, the local clusters $GaIn_3$, Ga_2In_2, and Ga_3In are also possible.

Thus each P-centered $Ga_{4-n}In_n$ cluster ($0 \le n \le 4$) has its own bond lengths $R^{(n)}_{Ga\text{-}P}$ and $R^{(n)}_{In\text{-}P}$, while only the averages $\langle R_{Ga\text{-}P} \rangle$ and $\langle R_{In\text{-}P} \rangle$ are measured. Extended x-ray-absorption fine-structure (EXAFS) experiments[11–13] showed that the A-C and B-C bond lengths in disordered $A_{1-x}B_xC$ semiconductor alloys are closer to the values in pure AC and BC compounds, respectively, than to the virtual lattice average. These experiments and subsequent modeling[14–17] have yielded a detailed picture of the nearest-neighbor environment in semiconductor alloys. However, a global picture of the atomic structure of semiconductor alloys, including the relaxation of further-neighbor pairs, bond angle distortions, and off-center displacements, is still lacking. This paper provides a general method capable of predicting such global structural features, as well as their effects on thermodynamic properties. Accurate local-density total energies of various ordered compounds are used to fit an effective interatomic potential. The latter is then used in continuous-space Monte Carlo (MC) simulations to obtain both $T=0$ and finite-temperature structural descriptions of the $Ga_{1-x}In_xP$ alloy. The predicted mixing enthalpy is close to that inferred from experiments. The calculated nearest-neighbor bond distances are in good accord with EXAFS data, and the predicted x-T phase diagram also agrees well with experiment. Having established this, we next move on to describe structural properties which are currently not amenable to measurement, including bond angle distributions, radial correlation functions, contour maps of atomic displacements in different crystal planes, and the effect of temperature on the above. Our detailed numerical results are then explained in terms of an analytical physical model. This establishes a global picture of the structure of substitutionally disordered semiconductor alloys.

II. THERMODYNAMIC DEFINITION OF THE ATOMIC STRUCTURE OF AN ALLOY

We start our discussion by introducing a thermodynamic description of the microscopic structure of a general pseudobinary $A_{1-x}B_xC$ alloy where the cation lattice is occupied by either A or B while the anion lattice is always occupied by C. Unlike the case of an ordered compound, where the lattice sites i are occupied by A or B atoms in a definite manner, the site occupations in a disordered alloy are merely probabilistic. It is therefore convenient to define pseudospin variables $\hat{S}_i$, taking up the values -1 or $+1$ if site i is occupied by A or B atoms, respectively. A lattice configuration σ is then a particular arrangement $\{\hat{S}_i\}$ of spins on the N lattice sites. There are 2^N such configurations. For each, we can define the excess internal energy

$$\Delta E(\sigma) \equiv E(\sigma) - (1-x)E(AC) - xE(BC) , \tag{2.1}$$

taken with respect to equivalent amount of pure AC and pure BC. The precise atomic positions $\{\mathbf{R}_i\}$ can deviate (relax) from the positions $\mathbf{R}_i^{(0)}$ of the rigid ideal lattice. Thus the excess energy $\Delta E(\sigma)$ of configuration σ is defined both by its spin-occupation numbers $\{\hat{S}_i\}$ (defining the topology) as well as by its atomic positions $\{\mathbf{R}_i\}$ (defining the precise geometry):

$$\Delta E(\sigma) = \Delta E[\{\hat{S}_i\};\{\mathbf{R}_i\}] . \tag{2.2}$$

The positional coordinates $\{\mathbf{R}_i\}$ include both cell external coordinates, (defining the lattice vectors of the repeat unit), as well as cell internal coordinates (defining the atomic position within the repeat unit).

The energies $\Delta E(\sigma)$ or bond length $R_{AA}(\sigma)$, $R_{BB}(\sigma)$, etc., of a particular configuration σ are generally not accessible to experimental tests, unless σ becomes a stable ordered structure, and unless a sample having a σ structure can be grown. For disordered or partially ordered phases γ, one must therefore average over the configurations σ according to

$$\langle \Delta E(\sigma) \rangle_\gamma = \sum_\sigma^{2^N} \Delta E(\sigma)\rho_\gamma(\sigma) , \tag{2.3a}$$

$$\langle R(\sigma) \rangle_\gamma = \sum_\sigma^{2^N} R(\sigma)\rho_\gamma(\sigma) , \tag{2.3b}$$

where $\rho_\gamma(\sigma)$ is the density matrix for the configuration σ in the ordered phase γ.[18] In a similar way, one can define the correlation functions $\{\xi_f^{(\gamma)}\}$ for phase γ and figure f (equal to pairs, three-body, four-body, ...) as the configuration average of the appropriate spin products.[6] For example, when f is a pair, the correlation function for sites i and j is $\langle \hat{S}_i\hat{S}_j \rangle$. As we will see below, the equilibrium value of the correlation functions depends on composition x and temperature T through the minimization of the free energy, so $\xi_f^{(\gamma)} = \xi_f^{(\gamma)}(x,T)$. For $T \to \infty$ all sites are uncorrelated [e.g., $\langle \hat{S}_i\hat{S}_j \rangle = \langle \hat{S}_i \rangle \langle \hat{S}_j \rangle$], and the alloy is said to be random. (Note that random implies absence of correlations or short-range order, while disordered permits such correlations.) At finite temperatures, there are correlations between the site occupancies, and $\{\xi_f^{(\gamma)}(x,T)\}$ can exhibit short-range order (SRO), long-range order (LRO), or both.

In general, the excess internal energy has both a configurational contribution ΔE_{config}, akin to a nonvibrating lattice, as well as a vibrational configuration ΔE_{vib} corresponding to the excess vibrational energy of σ relative to the constituent solids. The configurationally averaged excess internal energy for phase γ is

$$\begin{aligned}\langle \Delta E(\sigma) \rangle_\gamma = {} & \Delta E_{\text{config}}[\{\xi_f^{(\gamma)}(x,T)\};\{\mathbf{R}_i^\infty\}] \\ & + \Delta E_{\text{vib}}[\{\xi_f^{(\gamma)}(x,T)\};\{\mathbf{R}_i^\infty\}]\end{aligned} \tag{2.4}$$

where $\{\hat{S}_i\}$ of Eq. (2.2) has been replaced by the averaged quantities $\{\xi_f^{(\gamma)}\}$, and $\{\mathbf{R}_i^\infty\}$ represents the atomic positions of an infinite sample such that the configurational ergodicity is preserved. Similarly, the entropy has the same form:

$$\begin{aligned}\langle \Delta S(\sigma) \rangle_\gamma = {} & \Delta S_{\text{config}}[\{\xi_f^{(\gamma)}(x,T)\}] \\ & + \Delta S_{\text{vib}}[\{\xi_f^{(\gamma)}(x,T)\};\{\mathbf{R}_i^\infty\}] .\end{aligned} \tag{2.5}$$

We are now in a position to define the quantity indicated in the heading of this section: at a phase γ, the equilibrium structural parameters $\{\xi_f^{(\gamma)}\} + \{\mathbf{R}_i^\infty\}$ of an alloy with composition x and temperature T are those values

that minimize $F^{(\gamma)}=\langle \Delta E \rangle_\gamma - T\langle \Delta S \rangle_\gamma$:

$$F[\{\xi_f^{(\gamma)}(x,T)\};\{\mathbf{R}_i^\infty\}]=\min . \quad (2.6)$$

This thermodynamic definition of the structure of an alloy properly describes the configurational averaging needed; it includes both energetic and entropic terms, as well as configurational (i.e., spin), static-positional (i.e., relaxation), and vibrational (i.e., dynamic) effects.

For the ideal case of a perfectly random alloy, $S_{\text{config}}^{(R)}$ (R denotes random) is given by the structure-independent mean-field mixing entropy

$$S_{\text{config}}^{(R)}(x)=k_B[x\ln x+(1-x)\ln(1-x)] , \quad (2.7)$$

where k_B is Boltzmann's constant. Since $S_{\text{config}}^{(R)}$ does not depend on structure, the equilibrium $T=0$ geometry in mean-field theory is then obtained from

$$\Delta E_{\text{config}}^{(R)}[\{\mathbf{R}_i^\infty\}]+\Delta E_{\text{vib}}[\{\mathbf{R}_i^\infty\}]=\min . \quad (2.8)$$

Note that the correlation functions or the spin variables do not appear explicitly in Eq. (2.8) as they are assumed to be random. However, even though the site occupations are assumed random, the atomic positions that minimize Eq. (2.8) need not coincide with the ideal unrelaxed lattice sites. In order to calculate physical properties $P[\{\xi_f^{(\gamma)}(x,T)\};\ \{\mathbf{R}_i^\infty\}]$ using finite samples, the configurational ergodicity will be preserved only if $P[\{\xi_f^{(\gamma)}(x,T)\};\ \{\mathbf{R}_i^\infty\}]$ will be an average on sufficient different samples:

$$P[\{\xi_f^{(\gamma)}(x,T)\};\{\mathbf{R}_i^\infty\}]=\frac{1}{N}\sum_{j=1}^{N} P[\{\hat{S}_i^j(x,T)\};\{\mathbf{R}_i^j\}] . \quad (2.9)$$

This paper describes a practical way of calculating the free energy of semiconductor alloys in a general state of order $\{\xi_f^{(\gamma)}(x,T)\}$, and, through Eqs. (2.6)–(2.8), the atomic structure of such alloys. Before describing our own method, we will use the terminology introduced above to discuss previous approaches to this problem.

III. PREVIOUS METHODOLOGIES

Previous approaches that treat occupational and positional degrees of freedom simultaneously can be divided into direct methods which model directly the free energy vs $\{\hat{S}_i\}$ and $\{\mathbf{R}_i\}$, and cluster expansion (or Ising-like) methods which utilize a generalized Ising description in which atomic displacements do not appear explicitly. We next describe briefly the guiding principles of these methods, so we can place our own approach in proper perspective.

Most statistical-mechanics descriptions of chemical alloys $A_{1-x}B_x$ or spin alloys (ferromagnets or antiferromagnets) disregard the positional degrees of freedom $\{\mathbf{R}_i\}$, focusing only on the occupation degrees of freedom $\{\hat{S}_i\}$ or $\{\xi_f^{(\gamma)}\}$. The spins can be scalar Ising spins, or vector ones, and in some cases a combination.[19] These standard models have been reviewed, e.g., in Refs. 20 and 21. The underlying assumption in Ref. 21 is that atomic positions are invariant under changes in site occupations, specifically that the energy of a particular configuration is not affected much by the relaxation of the atoms off their ideal lattice sites. This appears to be physically unreasonable for alloys made of size mismatched constituents A and B: the atomic positions $\{\mathbf{R}_i\}$ of a structure with a small atom surrounded by large atoms must be different from that of a large atom surrounded by large atoms, etc. While off-lattice models were developed to study the phase-separating behavior of Si-Ge,[22,23] frozen-lattice alloy models continue to be used extensively for many alloy studies. The occupational degrees of freedom $\{\hat{S}_i\}$ are varied through Monte Carlo algorithms,[24,25] or the cluster variation method.[26] Zunger[27] recently reviewed evidence of the effects of positional relaxations on the thermodynamics of alloys, citing large, even qualitative changes in the phase diagram and all thermodynamic quantities. It thus appears that one must consider, in practical applications, both spin and atomic relaxations.

In the direct methods one models the four quantities of Eqs. (2.4) and (2.5) explicitly. An example is the method of Srolovitz and co-workers.[28–30] In this method, Eq. (2.6) is solved by assuming an ideal entropy of mixing for $S_{\text{config}}^{(R)}(x,\infty)$ [Eq. (2.7)], an Einstein model for $\Delta E_{\text{vib}}+TS_{\text{vib}}$, a mean-field virtual-crystal-like description of $\{\xi_f\}$, and an embedded-atom model[31] for $E[\{\hat{S}_i\};\{\mathbf{R}_i\}]$. Another example of a direct approach to this problem is the methods of Foiles[32] and Kelires and Tersoff,[33] who used a continuous-space grand-canonical Monte Carlo algorithm to equilibrate both the atomic positions $\{\mathbf{R}_i\}$ and the occupation variables $\{\hat{S}_i\}$ at a range of temperatures.

In the cluster expansion methods[20,21,26,27,33–35] one expands ΔE_{config} in a series of products $\xi_f J_f$, where J_f is the interaction energy of figure f, and ξ_f is its correlation function. This corresponds to a generalized Ising model in which multispin interactions are retained. The energies $\{J_f\}$ can be determined[27] from a series of total-energy calculations on atomically relaxed ordered phases. Thus J_f incorporates both spin-flip as well as relaxation effects (this often means that J_f depends on composition and volume, e.g., Ref. 6). Relaxation effects were introduced in Ising-like representations by Laks *et al.*[34] using a momentums-space formalism. A related cluster expansion approach is that of de Gironcoli, Giannozzi, and Baroni,[35] who expanded the energy of the alloy up to the second order with respect to the displacements $\{\mathbf{R}_i\}-\{\mathbf{R}_i^0\}$. In this approach, the electronic charge density and the forces were calculated using the Green's function linear-response theory, and $\{\mathbf{R}_i\}$ and $\{\hat{S}_i\}$ were calculated by Monte Carlo simulations. Both the methods of Laks *et al.*[34] and de Gironcoli, Giannozzi, and Baroni[35] permit full relaxations within an Ising representation.

Here we will use a direct approach which incorporates both spin and positional degrees of freedom without using an Ising expansion. Accurate $T=0$ local-density total energies of various ordered AC/BC structures are used to fit an effective interatomic potential. The latter is then used in continuous-space Monte-Carlo simulations.

Unlike Ising-based methods,[20,21] the convergence of a truncated Ising series is not involved. The main approximation is now the use of a parametrized Born-Oppenheimer surface $E[\{\hat{S}_i\};\{\mathbf{R}_i\}]$ without explicit electronic effects. Unlike the free-energy minimization method of Srolovitz and co-workers,[28–30] we used unapproximated S_{config}, E_{vib}, and S_{vib}. Unlike the Monte Carlo embedded-atom approach of Chakraborty and Xi,[31] we do include E_{vib} and S_{vib} terms neglected in Ref. 31.

IV. METHODS OF CALCULATION

A. Structural optimizations and finite-temperature Monte Carlo calculations

The excess configurational energy ΔE_{config} will be described here by an effective elastic potential which includes bond stretching and bond bending terms

$$\Delta E_{\text{config}}[\{\hat{S}_i\};\{\mathbf{R}_i\}]=\sum_{ij\in\sigma} V_{ij}+\sum_{ijk\in\sigma} V_{ijk} , \tag{4.1}$$

where V_{ij} and V_{ijk} are the two- and three-body interactions between the neighboring atoms i,j and i,j,k accordingly. The details of this potential are given in Sec. IV B, as is the description of its fitting to first-principles total-energy results.

The vibrational energy ΔE_{vib} and entropy ΔS_{vib} are included through a continuous-space Monte Carlo sampling in which a random spin configuration as well as a random displacement field are used to calculate the grand-canonical MC acceptance probabilities. The process is performed in the following steps.

(i) The initial spin configuration $\{\hat{S}_i\}$ is chosen so that the A/B sublattice is occupied randomly according to the alloy composition x. The initial atomic coordinates $\{\mathbf{R}_i\}$ are chosen as the zinc-blende position $\{\mathbf{R}_i^0\}$ of a cubic cell with periodic boundary conditions and a Vegard lattice constant $a(x)$.

(ii) The displacement field is defined as follows: first, atoms (indexed by i) are chosen randomly. After that three types of Monte Carlo displacements or flips are introduced: (a) At each step, a random and small coordinate displacement $\Delta\mathbf{R}_i$ is chosen, and the new positions $\{\mathbf{R}_i'\}$ are mapped: $\{\mathbf{R}_i'\}\rightarrow\{\mathbf{R}_i\}+\Delta\mathbf{R}_i$. (b) About every $1/P_S$ steps the spin $\hat{S}_i$ is flipped so $\{\hat{S}_i\}$ is mapped to $\{\hat{S}_i'\}$. (c) About every $1/P_V$ steps a random small volume change ΔV is chosen, and the volume of the cell is mapped by $\{\mathbf{R}_i'\}\rightarrow\{\mathbf{R}_i\}+\{\Delta\mathbf{R}_i\}$, where $\Delta\mathbf{R}_i=(1,1,1)\Delta V$ for all i. Hence P_S and P_V are the probabilities for the spin flip and volume change, respectively. We chose $P_S=0.05$ and $P_V=1/N$, where N is the number of atoms in the sample. We found that these are optimum values for stability as well as for fast convergence of the MC algorithm.

(iii) Each MC step is accepted with a probability P_{accept}, where

$$P_{\text{accept}}=\begin{cases}\exp(\delta E)/k_BT) & \text{if } \delta E>0\\ 1 & \text{otherwise} ,\end{cases} \tag{4.2}$$

where T is the temperature of the sample, and k_B is the Boltzmann constant. The energy change due to spin and position changes is

$$\delta E=\Delta E_{\text{config}}[\{\hat{S}_i'\};\{\mathbf{R}_i'\}]+\sum_i \mu_i(\hat{S}_i') -\Delta E_{\text{config}}[\{\hat{S}_i\};\{\mathbf{R}_i\}]-\sum_i \mu_i(\hat{S}_i) . \tag{4.3}$$

Here $\Delta E_{\text{config}}[\{\hat{S}_i\};\{\mathbf{R}_i\}]$ is calculated from Eq. (4.1), and $\mu_i(\hat{S}_i)$ is the chemical potential of the atom species $\hat{S}_i$, to be defined below. Procedures (ii) and (iii) define the MC step. In the multistep MC equilibration process, each site is relaxed individually while all other sites are held fixed. Each site change affects its four bond lengths, six bond angles, and the 12 angles of its nearest neighbors; thus the energy change is calculated only for the above. This method is very efficient, as was demonstrated by Weidmann and Newman,[36] and it was also used by Glas.[37]

We treat both disordered [Eq. (2.6)] and chemically random [Eq. (2.8)] cases. When disordered alloys are considered, the atomic configuration $\{\mathbf{R}_i\}$ as well as the spin configuration $\{\hat{S}_i\}$ are changed in a range of temperatures. This involves the calculations of $\{\mathbf{R}_i\}$ and $\{\hat{S}_i\}$ after the MC equilibration process described above, where μ_A and μ_B of Eq. (4.3) are the chemical potentials of species A and B in the alloy $A_xB_{1-x}C$. This calculation resembles the process of annealing a sample at a temperature T. The initial atomic configuration $\{\mathbf{R}_i\}$ is a zinc-blende structure, while the initial spin configuration $\{\hat{S}_i\}$ is chosen randomly. The phase diagram of a phase-separating alloy $A_xB_{1-x}C$ can now be calculated as described by Kelires and Tersoff.[23] The compositions $x_1(T)$ and $x_2(T)$ of the two coexisting phases at a temperature T are obtained by plotting the composition $\langle x(\Delta\mu,T)\rangle$ averaged over the MC iterations versus $\Delta\mu=\mu_A-\mu_B$. The average $\langle x(\Delta\mu,T)\rangle$ exhibits a first-order phase transition, where $x_1(T)$ and $x_2(T)$ are the coexisting compositions. Plotting $x_1(T)$ and $x_2(T)$ versus T gives the phase diagram.

When perfectly random alloys are considered, the (ideal) mixing entropy does not depend on the structure [Eq. (2.7)], so the equilibrium structure is decided by minimizing the internal energy without any spin flips. Thus, when perfectly random alloys are considered, δE of Eq. (4.3) is evaluated at a constant (random) spin configuration corresponding to a given composition x. This calculation resembles the process of quenching a sample which was initially equilibrated at some high temperature.

In either cases, the samples used in the present calculations consisted of periodically repeated cubic cells of $8\times N\times N\times N$ atoms for $N=5$. In order to accumulate enough statistics for the structural properties, some 200 such samples with different spin configurations $\{\hat{S}_i\}$ were equilibrated for each case. We also checked for finite-size effects by the calculation of selected points using our two basic algorithms: (i) internal energy minimization without any spin flips, and (ii) the MC equilibration process at $T>0$ with spin flips. Using cubic cells of $8\times N\times N\times N$ atoms for $5\le N\le 8$, we estimate that finite-size errors are below 1% for both algorithms.

B. Fitting the ternary valence force field (VFF) to first-principles calculations

The methodology described above will be applied in what follows to AC=GaP, BC=InP alloys which have received prominence due to their applications in photovoltaic solar cells,[38] high-power quantum-well lasers,[39] light-emitting diodes,[40] and high electron mobility transistors.[41] In addition, experimental data exist for the alloy bond lengths,[11] mixing enthalpies,[42,43] and the phase diagram.[44] Previous theoretical results include calculations of alloy bond lengths using local-density-approximation (LDA) calculations,[45,46] the radial force model,[47] tight-binding perturbation theory,[48] valence-force-field calculations,[14] and empirical potential calculations.[49,50] In addition, cluster expansion calculations of thermodynamic properties have been reported in Refs. 34 and 51.

The excess configurational energy $\Delta E^{(\sigma)}_{\text{config}}$ of Eq. (4.1) is modeled here by the valence force field (VFF) of Keating[52] (see also Refs. 14 and 53):

$$\Delta E^{(\sigma)}_{\text{config}}=\sum_l \sum_{m=1}^{4} \frac{3}{8d_{AC}^2}\alpha_{AC}[\mathbf{r}_m(l,1)\cdot\mathbf{r}_m(l,1)-d_{AC}^2]^2 + \sum_l \sum_{s=1}^{2} \sum_{m=1}^{3} \sum_{n=m+1}^{4} \frac{3}{8d_{AC}^2}\beta_{A-C-A}\left[\mathbf{r}_m(l,s)\cdot\mathbf{r}_n(l,s)+\frac{d_{AC}^2}{3}\right]^2 \tag{4.4}$$

where $d_{AC}=R_{ij}^0$ is the equilibrium interatomic distance in the binary constituents, $\mathbf{r}_m(l,s)$ is the vector connecting atom s in unit cell l to its mth nearest neighbor, and α_{AC} and $\beta_{A\text{-}C\text{-}A}$ are the bond-stretching and bond-bending force constants, respectively. Note that ΔE_{config} is the excess energy of Eq. (2.1), so $\Delta E_{\text{config}}(AC)\equiv\Delta E_{\text{config}}(BC)\equiv 0$ since in the binary compounds AC and BC $d_{AC}=R_{ij}^0$, and all bond angles are the tetrahedral angles $\theta_{ijk}^0=109.47°$ [i.e., $\mathbf{r}_m(l,s)\cdot\mathbf{r}_n(l,s)/d_{AC}^2=-\frac{1}{3}$]. In order to achieve physical values for the chemical potential difference $\Delta\mu(T)$ during the phase-diagram calculations (see Sec. IV A), scaling of the excess energies of the binary compounds $E(AC)$ and $E(BC)$ to their physical values is required. This scaling does not change the resulting x-T phase diagram but only the values of $\Delta\mu(T)$. To this end we added to Eq. (4.4) the experimental bond energies of GaP and InP:

$$E_{\text{config}}(\sigma)=\Delta E_{\text{config}}(\sigma)+(1-x)E(AC)+xE(BC)\ , \tag{4.5}$$

where

$$E(AC)=\sum_l \sum_{m=1}^{4} E_m(l,s)\ . \tag{4.6}$$

$E_m(l,s)$ is the ideal binary zinc-blende energy of the bond connecting atom s in its unit cell l to its mth neighbor. We took $E_m(l,s)=-1.78$ eV/bond for Ga-P and $E_m(l,s)=-1.74$ eV/bond for In-P.[54]

The VFF potential of Eqs. (4.4)–(4.6) is applicable only to fourfold-coordinated systems with small bond-length or bond angle deformations, but cannot handle broken-bond configurations or charge-dependent structural changes. The latter is, however, not required in the present work. Martin[53] calculated the values of α and β of Eq. (4.4) for binary AC and BC materials. Since the original VFF correctly predicted the elastic coefficients of the binary compounds InP and GaP, we leave the binary β's unchanged. For the ternary $A_xB_{1-x}C$ compound, Martin[53] suggested the relations

$$\begin{aligned}\beta_{A\text{-}C\text{-}A}&=\beta_{C\text{-}A\text{-}C}\ ,\\ \beta_{B\text{-}C\text{-}B}&=\beta_{C\text{-}B\text{-}C}\ ,\\ \beta_{A\text{-}C\text{-}B}&=\tfrac{1}{2}(\beta_{A\text{-}C\text{-}A}+\beta_{B\text{-}C\text{-}B})\ .\end{aligned} \tag{4.7}$$

Generalizing this, we introduce different parameters β for the ternary alloy, namely $\beta_{A\text{-}C\text{-}A}$, $\beta_{C\text{-}A\text{-}C}$, $\beta_{B\text{-}C\text{-}B}$, $\beta_{C\text{-}B\text{-}C}$, and $\beta_{A\text{-}C\text{-}B}$. Figure 1 illustrates these parameters for A=In, B=Ga, and C=P. We parametrize these β values as

$$\begin{aligned}\beta_{\text{P-In-P}}&=(1+f_{\text{In}})\beta_{\text{In-P}}\ ,\\ \beta_{\text{In-P-In}}&=(1-f_{\text{In}})\beta_{\text{In-P}}\ ,\\ \beta_{\text{Ga-P-Ga}}&=(1+f_{\text{Ga}})\beta_{\text{Ga-P}}\ ,\\ \beta_{\text{P-Ga-P}}&=(1-f_{\text{Ga}})\beta_{\text{Ga-P}}\ .\end{aligned} \tag{4.8}$$

Note that the In-P-Ga bond angle does not occur in binary compounds. It is easy to verify from Eqs. (4.8) that using the binary $\beta_{A\text{-}C\text{-}A}$, $\beta_{B\text{-}C\text{-}B}$, and the three new parameters $\{\beta_{\text{In-P-Ga}},f_{\text{In}},f_{\text{Ga}}\}$ does not change the VFF elastic constants for the binary compounds.

The ternary force constants of Eqs. (4.8) were fit to first-principles total-energy calculations on ordered periodic structures.[55] Most of these structures can be described[56] as $(AC)_p/(BC)_q$ superlattices of periods (p,q) and direction $\hat{G}$, except for two structures, $L1$ and $L3$, which are not superlattices. The fully relaxed excess energies $\{\Delta E_{\text{LDA}}(s,V)\}$ [Eq. (2.1)] of 25 ordered structures $\{s\}$ of the $(\text{GaP})_p/(\text{InP})_q$ compounds were calculated[55] in the local-density approximation (LDA) as implemented by the general-potential, linear augmented-plane-wave (LAPW) method.[57] (The calculations of Ref. 51 have been refined in Ref. 55 by adding more **k** points, using better basis set convergence, and adding many more structures.) Using Eqs. (4.4) and (4.8) we have also calculated the excess energies of the ordered structures

$\{\Delta E_{\rm VFF}(s,V,\beta_{\rm In\text{-}P\text{-}Ga},f_{\rm In},f_{\rm Ga})\}$. For each of the structures, the excess energy of the relaxed cell was calculated where the cell external coordinates (i.e., the 3×3 matrix which describes the parallelepiped shaped unit cell) as well as the cell internal coordinates (i.e., the atomic coordinates tensor) were relaxed using a Monte Carlo algorithm at $T=0$. To fit the VFF to the LDA, we define a cost function which expresses the difference between the VFF and LDA excess energies as a function of the three parameters $\beta_{\rm In\text{-}P\text{-}Ga}$, $f_{\rm In}$, and $f_{\rm Ga}$:

$$C(\beta_{\rm In\text{-}P\text{-}Ga},f_{\rm In},f_{\rm Ga})=\sum_{\substack{\text{ordered}\\ \text{structure}}}|\Delta E_{\rm LDA}(s,V)-\Delta E_{\rm VFF}(s,V,\beta_{\rm In\text{-}P\text{-}Ga},f_{\rm In},f_{\rm Ga})|\ . \tag{4.9}$$

A simulated annealing algorithm[58] was used to find values of the parameters which minimize $C(\beta_{\rm In\text{-}P\text{-}Ga},f_{\rm In},f_{\rm Ga})$.

The surface of the cost function $C(\beta_{\rm In\text{-}P\text{-}Ga},f_{\rm In},f_{\rm Ga})$ is complex, having many local minima. In some cases, the simulated annealing algorithm reached minima with $|f_{\rm In}|>1$ or $|f_{\rm Ga}|>1$, resulting [see Eqs. (4.8)] in unphysical negative values of one of the bond bending force constants $\beta_{A\text{-}C\text{-}A}$. We regarded these local minima of $C(\beta_{\rm In\text{-}P\text{-}Ga},f_{\rm In},f_{\rm Ga})$ as forbidden minima, so we add to the cost function a constraint function, multiplied by a Lagrange multiplier,

$$C'(\beta_{\rm In\text{-}P\text{-}Ga},f_{\rm In},f_{\rm Ga})=C(\beta_{\rm In\text{-}P\text{-}Ga},f_{\rm In},f_{\rm Ga})+\lambda(h_{\rm In}+h_{\rm Ga})\ , \tag{4.10}$$

where h_A represents the functions:

$$h_A=\begin{cases}0 & \text{if } -1\le f_A\le 1\\ 1 & \text{otherwise}\ .\end{cases} \tag{4.11}$$

In this way, the modified cost function C' is allowed to pass through the forbidden minima, but it is most probable that it will not stay there. The value of the Lagrange multiplier λ was chosen to be comparable to the depth of the valleys of C (~5 meV), as observed during test runs of the simulated annealing algorithm.

The best-fit values for the parameters of Eq. (4.8) were

$$\begin{aligned}\beta_{\rm In\text{-}P\text{-}Ga}&=1.6715N/m\ ,\\ f_{\rm Ga}&=-0.4621\ ,\\ f_{\rm In}&=0.9705\ .\end{aligned} \tag{4.12}$$

The resulting β values are given in the inset of Fig. 1. Since our VFF is fit also to ternary (T) data, we will refer to it as T-VFF, to be distinguished from the Keating-Martin binary VFF. Tables I and II compare the LDA values of $\Delta E(s,V_{\rm eq})$ to the fitted T-VFF values. We see that the current T-VFF potential considerably improves the overall fit compared to the original VFF potential. This is particularly true for the superlattice structures in orientations [110], [201], and [113], where the fit of the original VFF potential is quite poor. The fit of the original VFF potential for the superlattice structures in orientations [111] and [001] and for the Luzonite structures (Table II) is very good; our fit thus leaves these values essentially unchanged. The existence of a small rms error over a wide range of compositions and superlattice orientations (Tables I and II) suggests that our T-VFF can also be used to predict energies of structure outside the set $\{\hat{S}\}$ used in the fit.

The only other elastic potential for the GaP-InP that we are aware of is that of Khor and Das Sarma (KDS).[49] We have compared its predictions to those of T-VFF and found (Table I) that they are consistently inferior. Even modifications of this potential to a similar form to the improved version for Si-Ge interactions[59,60] (M-KDS in Table I, described in Appendix A) do not give sufficiently accurate results. We thus use T-VFF.

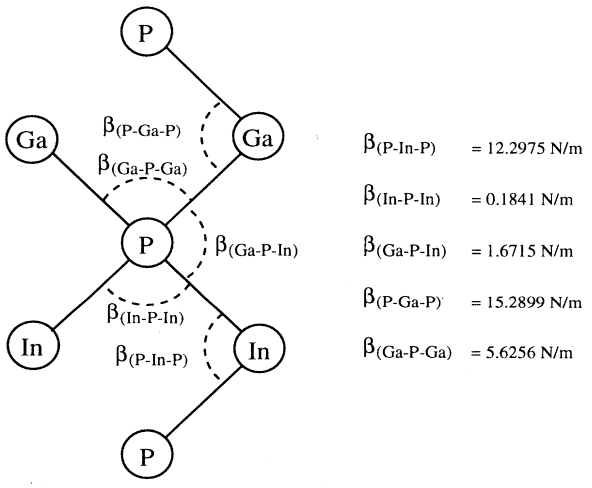

FIG. 1. Schematic diagram depicting the different bond-bending force constants in the $Ga_{1-x}In_xP$ random alloy. The five force constants β of the VFF potential are labeled. The best values found in our fit to the LAPW results are given.

V. RESULTS: COMPARISON WITH MEASURED THERMODYNAMIC AND STRUCTURAL PROPERTIES

A. Mixing enthalpy of the chemically random alloy

Equation (2.4) defines the mixing enthalpy (excess internal energy) of the disordered alloy, which we will denote here as $\Delta H_{\rm mix}(x,T)$. The formation enthalpy of ordered compounds is denoted ΔH_F. Figure 2 shows $\Delta H_{\rm mix}(x,T=\infty)$ for the $Ga_{1-x}In_xP$ alloy neglecting vibrational effects. $T=\infty$ denotes perfectly random substitution in the mixed sublattice. We give results with atomic relaxation (dashed line), and without relaxation (solid line). The asterisks denote the formation enthalpies

TABLE I. Formation enthalpies ΔH for ordered structures of InP/GaP, where A=GaP and B=InP. The structures are described as $(AC)_p(BC)_q$ superlattices with layer repeats (p,q) and orientation G. The formation enthalpies were calculated using LDA, the original Keating VFF potential (VFF) (Refs. 52 and 53), our ternary potential (T-VFF), the potential of Khor and Das Sarma (KDS) (Ref. 49), and our modified KDS potential (M-KDS). The units are meV/four atoms, and the symbols define structure names (as defined in Ref. 55).

Formula	Potential	Orientation [111]	[001]	[110]	[201]	[113]	Row average deviation[a]
AB		CP	CA	CA	CA	CP	
	LDA	144.2	90.3	90.3	90.3	144.2	
	T-VFF	132.4	93.5	93.5	93.5	132.4	6.6
	VFF	133.6	87.5	87.5	87.5	133.6	5.9
	KDS	98.7	83.8	83.8	83.8	98.7	22.1
	M-KDS	86.7	84.1	84.1	84.1	86.7	26.7
AB_2		$\alpha 1$	$\beta 1$	$\gamma 1$	$\gamma 1$	$\gamma 1$	
	LDA	128.0	81.9	46.6	46.6	46.6	
	T-VFF	127.4	90.8	43.6	43.6	43.6	5.0
	VFF	128.7	87.3	58.9	58.9	58.9	9.8
	KDS	94.0	86.5	104.9	104.9	104.9	47.1
	M-KDS	88.0	85.5	98.1	98.1	98.1	45.0
A_2B		$\alpha 2$	$\beta 2$	$\gamma 2$	$\gamma 2$	$\gamma 2$	
	LDA	126.7	79.1	45.6	45.6	45.6	
	T-VFF	109.1	77.2	45.7	45.7	45.7	5.0
	VFF	109.7	72.8	59.4	59.4	59.4	14.9
	KDS	30.9	26.0	59.3	59.3	59.3	47.4
	M-KDS	38.3	32.4	58.9	58.9	58.9	44.0
AB_3		$V1$	$Z1$	$Y1$	$F1$	$W1$	
	LDA	110.4	72.9	54.3	32.0	62.9	
	T-VFF	112.4	80.3	53.6	34.0	63.8	4.6
	VFF	113.5	78.0	60.8	43.6	72.0	10.9
	KDS	66.3	61.8	90.8	68.6	99.9	45.8
	M-KDS	62.1	61.0	76.8	66.9	82.0	35.9
A_2B_2		$V2$	$Z2$	$Y2$	CH	$W2$	
	LDA	141.8	90.6	60.7	29.8	61.0	
	T-VFF	132.1	94.1	60.2	40.2	62.4	6.0
	VFF	132.6	91.1	78.1	57.1	75.8	16.0
	KDS	44.6	41.5	84.4	91.9	86.9	60.8
	M-KDS	51.1	47.1	76.9	85.7	83.6	53.0
A_3B		$V3$	$Z3$	$Y3$	$F3$	$W3$	
	LDA	105.1	67.7	54.9	45.3	69.6	
	T-VFF	88.7	62.7	58.1	52.2	67.8	6.9
	VFF	89.1	59.4	64.1	61.0	74.7	13.2
	KDS	20.9	19.6	44.3	98.2	53.3	51.3
	M-KDS	34.6	29.5	48.6	78.9	51.5	44.2
Column average deviation[b]							
	T-VFF	9.7	5.0	1.8	4.3	3.2	
	VFF	9.4	4.7	10.3	13.9	11.0	
	KDS	66.8	28.8	24.9	38.4	32.8	
	M-KDS	65.9	25.0	19.3	32.6	30.4	

[a]The average deviations relative to the LDA values for the rows.
[b]The average deviations relative to the LDA values for the columns.

TABLE II. Formation enthalpies ΔH for the two luzonite-ordered structures of $Ga_{1-x}In_xP$, where A=GaP and B=InP. The formation enthalpies were calculated using LDA, our ternary potential (T-VFF), Keating original VFF potential (VFF), the pseudopotentials of Khor and Das Sarma (KDS), and our modified KDS potential (M-KDS). The units of the formation enthalpies are meV/four atoms.

Formula	Name	Potential	ΔH
AB_3	$L1$	LDA	57.4
		T-VFF	60.7
		VFF	57.1
		KDS	68.8
		M-KDS	69.2
A_3B	$L3$	LDA	77.9
		T-VFF	81.8
		VFF	80.8
		KDS	111.4
		M-KDS	88.0

ΔH_F of some of the ordered structures, defined in Table I.

The unrelaxed (ur) mixing enthalpy ΔH^{ur}_{mix} was calculated directly from Eq. (4.4). In this geometry, all bonds have the same length, and all bond angles equal the tetrahedral value $\theta^0_{ijk}=109.47°$. ΔH^{ur}_{mix} is therefore

$$\Delta H^{ur}_{mix}(x)=x\Delta E_{InP}[R(x)]+(1-x)\Delta E_{GaP}[R(x)] , \tag{5.1}$$

where $R(x)$ is the average bond length given by the linear relation

$$R(x)=xR^0_{InP}+(1-x)R^0_{GaP} , \tag{5.2}$$

and $\Delta E[R(x)]$ is calculated using the two-body term of Eq. (4.4). The relaxed (r) mixing enthalpy ΔH^r_{mix} was calculated by minimizing the formation enthalpy of $Ga_{1-x}In_xP$ samples relative to the atomic configuration $\{\mathbf{R}_i\}$, starting from an initial zinc-blende structure, where the spin configuration $\{\hat{S}\}$ was chosen randomly according to the required composition x. Relaxation lowers ΔH_{mix} enormously: The maximum value for the relaxed system $\Delta H^r_{mix}(x=0.47,T=\infty)=77.1\pm0.1$ meV/four atoms is much lower than the unrelaxed value $\Delta H^{ur}_{mix}(x=0.53,T=\infty)=304\pm1$ meV/four atoms.

Only indirect measurements exist for ΔH_{mix} in $Ga_{1-x}In_xP$. The reduced enthalpy (interaction parameter)

$$\hat{\Omega}(x,T)=\Delta H(x,t)/x(1-x) \tag{5.3}$$

was estimated in these experiments by fitting the observed liquidus and solidus lines to simple thermodynamic models. This gives $\hat{\Omega}(x=0.5,T=800\ \text{K})=3.40$,[61] 3.5,[42] 3.575,[43] and 3.25 kcal/mol,[62] while our result of the relaxed system is $\hat{\Omega}(x=0.5,T=\infty)=3.33$ kcal/mol, and the estimate of Bublik and Leikin[63] is $\hat{\Omega}(x=0.5,T=\infty)=4.05$ kcal/mol. The cluster expansion (CE) calculation based on the local-density approximation gives $\hat{\Omega}(x=0.5,T=\infty)=3.82$ kcal/mol,[34] and $\hat{\Omega}(x=0.5,T=800\ \text{K})=3.07$ kcal/mol.[51] Numerical simulations gives $\hat{\Omega}(x=0.5,T=\infty)=3.77$ kcal/mol.[34] Note also that in Fig. 2 the ΔH_F of some of the ordered structures is below ΔH^r_{mix}, which means that at low temperatures these ordered structures are more stable than the random alloys.

If $\Delta H_{mix}(x)$ were parabolic, the interaction parameter $\hat{\Omega}(x)$ would be x independent. Fitting our $\Delta H^r_{mix}(x)$ to Eq. (5.3) shows, however, a nearly linear behavior $\hat{\Omega}(x)=\Omega_0+ax$. Our fit is

$$\hat{\Omega}(x,T=\infty)=3.7-0.8x(\text{kcal/mol}) , \tag{5.4}$$

while Bubik and Leikin[63] have estimated

$$\hat{\Omega}(x,T=\infty)=4.6-1.1x(\text{kcal/mol}) \tag{5.5}$$

using x-ray diffuse scattering results and the measured composition dependency of the elastic constants of $Ga_{1-x}In_xP$. Both estimations indicate that $\Delta H_{mix}(x)$ is not symmetric about $x=\frac{1}{2}$. Interestingly, for the relaxed alloy, the slope a of $\hat{\Omega}(x,T=\infty)$ satisfies $a<0$, while for the unrelaxed alloy $a>0$ (compare the solid line to the dashed line in Fig. 2). Indeed $\lim_{x\to0}\hat{\Omega}(x)$ and $\lim_{x\to1}\hat{\Omega}(x)$ are the limiting solution enthalpy representing the change in enthalpy when impurity amounts of A are added to BC. Our result thus indicates that, for the unrelaxed alloy,

$$\Delta H^{ur}_{mix}(\text{GaP:In})<\Delta H^{ur}_{mix}(\text{InP:Ga}) . \tag{5.6}$$

Thus it costs less energy to dissolve a large atoms (In) in a small host (GaP) than to dissolve a small atom (Ga) in a large host (InP). However, the opposite is true when relaxation is allowed, i.e.,

$$\Delta H^r_{mix}(\text{GaP:In})>\Delta H^r_{mix}(\text{InP:Ga}) . \tag{5.7}$$

This result implies that the effective (eff) force constant of the In-P bond within the GaP host is higher than the Ga-P bond within the InP host:

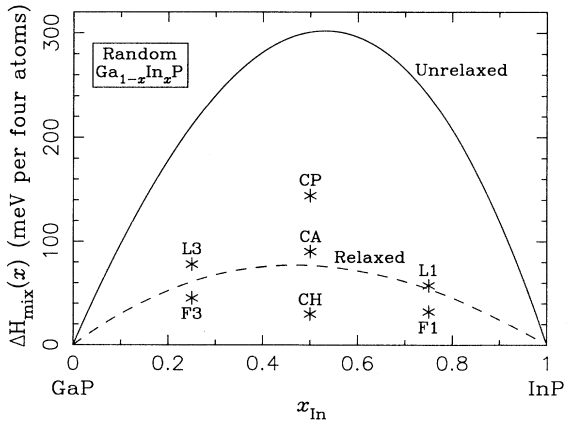

FIG. 2. The mixing enthalpy of the chemically random $Ga_{1-x}In_xP$ alloy. The solid line denotes the unrelaxed results, while the dashed line denotes the relaxed mixing enthalpy. The asterisks denotes the formation enthalpies of some ordered structures defined in Table I.

$$\alpha^{\text{eff}}_{\text{In-P}}(\text{GaP}) > \alpha^{\text{eff}}_{\text{Ga-P}}(\text{InP}) \ . \tag{5.8}$$

This is the reverse of the situation in the pure binary materials, where the VFF values are[14]

$$\alpha_{\text{In-P}} < \alpha_{\text{Ga-P}} \ . \tag{5.9}$$

B. The finite-temperature phase diagram

Figure 3 shows the x-T phase diagram of the $Ga_{1-x}In_xP$ alloy. The circles connected by dashed lines denote the results of the MC calculations (interpolated near the top of the miscibility gap), while the squares denotes the recent experimental results of Ishida *et al.*[44]

It is interesting to compare the values of the critical temperature (T_{MG}) and composition (x_{MG}) obtained by different statistical approximations to our approach. Table III lists a hierarchy of approximations that are in common use. They can be divided into (i) approximations to the excess enthalpy ΔH, (ii) approximations to the configurational entropy ΔS_{config}, and (iii) approximations to vibrational quantities ΔH_{vib} and ΔS_{vib}. These approximations can be conveniently described by using a stepwise breakdown of the terms entering the free energy of the disordered alloy in Eqs. (2.4)–(2.7):

$$\begin{aligned}\Delta F(x,T) = &[\Delta E^{(R)}_{\text{config}}(x,\infty) - TS^{(R)}_{\text{config}}(x,\infty)] \\ &+ [\Delta E_{\text{config}}(x,T) - \Delta E^{(R)}_{\text{config}}(x,\infty)] \\ &- T[S_{\text{config}}(x,T) - S^{(R)}_{\text{config}}(x,\infty)] \\ &+ [\Delta E_{\text{vib}}(x,T) - T\Delta S_{\text{vib}}(x,T)] \ . \end{aligned} \tag{5.10}$$

The first term contains the configurational enthalpy and entropy, both evaluated by assuming that each lattice site is occupied randomly by A or B, i.e., a mean-field approach. All correlations and vibrations are ignored in this mean-field approach. The second term of Eq. (5.10) represents the correction due to nonrandomness (i.e., SRO) to the enthalpy, while the third term gives a nonrandomness correction to the entropy. Finally, the fourth term represents vibrational effects.

We can now explain the various approximations (i)–(v) of Table III.

(i) In the first approximation one retains only the first bracketed term of Eq. (5.10), i.e., one assumes that both ΔH and ΔS can be taken from a perfectly random atomic arrangement using a mean-field description. Here one neglects the temperature and composition dependences of $\hat{\Omega}(x,T)$ [Eq. (5.3)], and uses an unrelaxed lattice. Fitting the solid line of Fig. 2 to a parabola gives $\hat{\Omega}=13.88$ kcal/mol for this random, unrelaxed lattice. The phase diagram is symmetric about $x=\frac{1}{2}$ and shows $T_{\text{MG}}=3495$ K and $x_{\text{MG}}=0.5$.

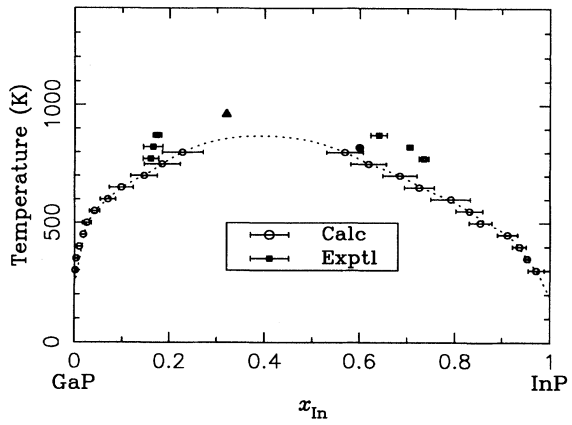

FIG. 3. Calculated and measured (Ref. 44) x-T phase diagram of the disordered $Ga_{1-x}In_xP$ alloy. The open circles denote the results of our Monte Carlo simulations, and the dashed line is an interpolation of these results. The squares denote the experimental results (Ref. 44), and the filled circle and triangle denote the maximum miscibility-gap temperature of the *ab initio* calculations of Marzari, Gironcoli, and Baroni (Ref. 68) and Wei, Ferreira, and Zunger (Ref. 51).

(ii) In the second approximation one relaxes the lattice. This affects ΔH but not ΔS. A parabolic fit to the dashed line of Fig. 2 gives $\hat{\Omega}=3.31$ kcal/mol. This relaxation-induced lowering of $\hat{\Omega}$ lowers also T_{MG} to 833 K. Approaches (i) and (ii) comprise the regular solution model, and are used widely in the literature[42,43,61] in conjection with empirical $\hat{\Omega}$ values. We see that relaxation has an enormous effect on T_{MG}. It is ignored in most Ising-type treatments of alloys,[20,21] as reviewed recently.[27]

(iii) In the third approximation one permits $\Delta H_{\text{mix}}(x)$ to be asymmetric with respect to $x=\frac{1}{2}$. A fit of the relaxed $\Delta H_{\text{mix}}(x)$ of Fig. 2 then gives $\hat{\Omega}=3.7-0.8x$ kcal/mol. A phase-diagram calculation using the common tangent method[64] gives $T_{\text{MG}}=912$ K and $x_{\text{MG}}=0.43$. Thus the asymmetry in the phase diagram comes from the asymmetry in ΔH_{mix}. The effect on T_{MG} is, however, rather small.

(iv) In the fourth approximation one permits atomic correlations (i.e., short-range order effects) in both ΔE and ΔS, while still neglecting vibrational effects. This

TABLE III. Different approximation to the upper miscibility temperature T_{MG} and composition x_{MG}. All approximations are based on the present interatomic T-VFF potential (see Sec. V B).

Method	$\{\mathbf{R}_i\}$	$\hat{\Omega}$	$\{\hat{S}\}$	ΔS_{vib}	$T_{\text{MG}}(K)$	x_{MG}
(i)	Unrelaxed	x-indep.	Random	Zero	3495	0.50
(ii)	Relaxed	x-indep.	Random	Zero	833	0.50
(iii)	Relaxed	x-depend.	Random	Zero	912	0.43
(iv)	Relaxed		Nonrandom	Zero	900±40	0.42±0.03
(v)	Relaxed		Nonrandom	Nonzero	870±20	0.40±0.02

can be calculated by allowing spin flips as well as complete atomic relaxations in the MC runs to the lowest energy of each spin configuration (this is distinguished from continuous-space MC where atoms are displaced along random directions, which is not necessarily energy lowering). Note that atomic correlations tend to reduce the entropy relative to the mean-field value and (for phase-separating systems) also make the enthalpy less positive.[51] Since $T_{MG} \propto \Delta H/\Delta S$, these correlation effects in ΔH and ΔS can have opposite influences on T_{MG}. Using our T-VFF, we find that at this level of approximation $T_{MG}=900\pm40$ K and $x_{MG}=0.42\pm0.03$, so the net effect of atomic correlations is to lower the miscibility temperature. The calculation of Wei, Ferreira, and Zunger,[5] yielding $T_{MG}=961$ K and $x_{MG}=0.324$, corresponds to this approximation (however, these authors used the cluster variation method rather than the MC, and evaluated the energies from a cluster expansion of LDA results rather then from the VFF).

(v) In the final step one introduces vibrational effects through the use of random displacements. This lowers T_{MG} to 870 ± 20 K and moves x_{MG} to 0.40 ± 0.02. The results of this calculation is shown in Fig. 3. Thus vibrations tend to lower T_{MG}. The same trend was observed in empirical models that introduce vibrational effects into semiconductor alloy phase-diagram calculations.[65,66]

Bublik and Leikin[63] estimated $T_{MG}=996$ K and $x_{MG}=0.412$. From the spinodal isotherms of Onabe (Fig. 1 in Ref. 67), we estimated $T_{MG}\sim870$ K and $x_{MG}\sim0.5$. Recently calculated *ab initio* values by Marzari, de Gironcoli, and Baroni[68] yielded $T_c=820$ K and $x_c=0.6$ using Monte Carlo simulations based on the LDA to density-functional perturbation. The experimental results of Ishida *et al.*[44] (filled squares in Fig. 3) show a similar asymmetry in the phase diagram, but it is difficult to interpolate T_{MG} and x_{MG} from these results.

In summary, we see that the largest effect is that of inclusion of relaxation ($\sim80\%$ lowering of T_{MG}), and that statistical correlations and vibrations lower T_{MG} by 43 and 30 K, respectively. The most sophisticated calculation [method (v)] gives a value for T_{MG} that is ~40 K below that of the standard approach [method (iii)].

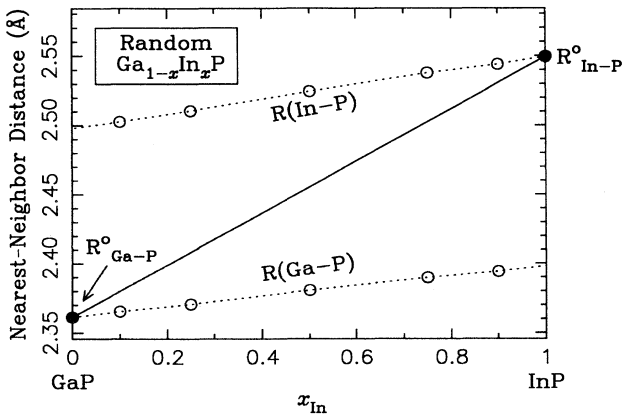

FIG. 4. The average anion-cation nearest-neighbor distance $\langle R_{A\text{-}C}(x)\rangle$ of the chemically random $Ga_{1-x}In_xP$ alloy. The open circles denote our average values, while the solid circles denote the bond length $R^0_{A\text{-}C}$ of the binary compounds GaP and InP. The solid line is the Vegard law prediction.

TABLE IV. Experimental EXAFS results vs ours and other model calculations of the first-nearest-neighbor bond length change Δ_{AC} in the ideally random $Ga_{1-x}In_xP$ alloy on going from $x\to1$ to $x\to0$. Δ_{AC} is defined in Eq. (5.11).

	Δ_{GaP} Å	Δ_{InP} Å	rms deviation[a] Å
Experiment[b]	0.038	0.044	
Present work	0.036	0.050	0.006
Radial force model[c]	0.045	0.045	0.007
Perturbation theory[d]	0.036	0.054	0.010
VFF[e]	0.049	0.067	0.025

[a]The rms deviation between the theoretical and experimental results.
[b]Reference 11.
[c]Reference 47.
[d]Reference 48.
[e]Reference 14.

C. Nearest-neighbor bond lengths

Figure 4 depicts the average nearest-neighbor bond lengths $R_{Ga\text{-}P}(x)$ and $R_{In\text{-}P}(x)$ versus x in the random alloy $Ga_{1-x}In_xP$. Table IV summarizes the bond-length changes Δ_{AC} for $A=$In or Ga and $C=$P where

$$\Delta_{AC}=\lim_{x\to1}R_{AC}(A_xB_{1-x}C)-\lim_{x\to0}R_{AC}(A_xB_{1-x}C) \tag{5.11}$$

is the slope of the dashed lines in Fig. 4. The values of the present work are compared in the table with experimental EXAFS results[11] and with other theoretical results, e.g., the radial force model of Shin *et al.*,[47] the original form of the VFF potential,[14] and the tight-binding perturbation theory results of Chen and Sher.[48] Our results and those of Shin *et al.*[47] are the closest to the experimental values.

VI. PREDICTED ATOMIC GEOMETRY IN THE CHEMICAL RANDOM ALLOY

Having established the adequacy of our model to describe measurable alloy properties we next use our model to predict currently unmeasured properties, in particular, structural quantities. We focus first on chemical random alloys without SRO or LRO. We thus minimize $E_{config}[\{\mathbf{R}_i\}]$ at $\{\xi_f\}\equiv\{\xi_f^{random}\}$.

A. Nearest-neighbor bond-length distribution

Figure 5 depicts the nearest-neighbor distance distribution of the chemically random $Ga_{1-x}In_xP$ alloy. The solid line histograms denote model calculations described in Appendix B, while the shaded histograms describe the results of our statistical simulations of random alloys relaxed at $T=0$ K. The dashed lines denote the bond

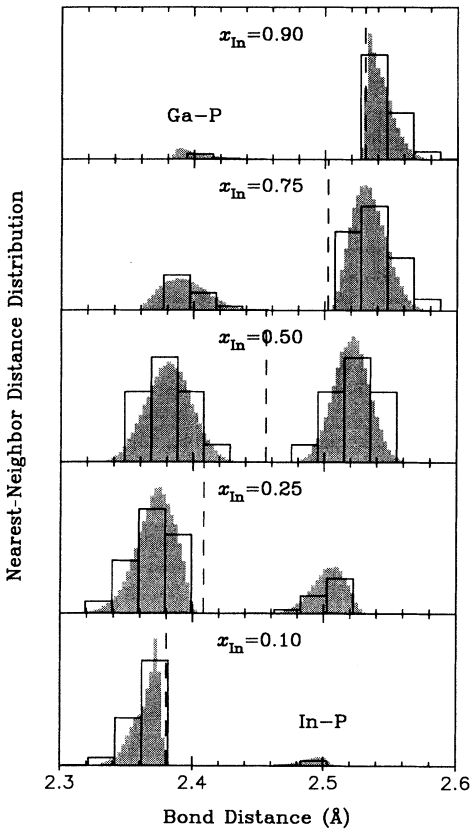

FIG. 5. Histogram plots of the nearest-neighbor distance distributions of the chemically random $Ga_{1-x}In_xP$ alloy for five In compositions. The solid line histograms denote the model calculation described in Sec. VI A, while the shaded histograms denote the results of numerical simulations on samples relaxed at $T=0$ K. The dashed vertical lines denote the bond lengths in the virtual alloy of composition x, calculated according to $r(x)=xr_{A\text{-}C}+(1-x)r_{B\text{-}C}$.

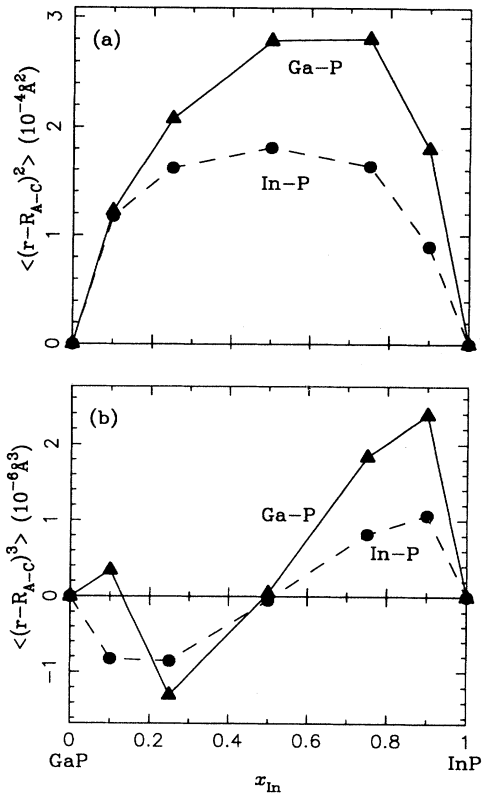

FIG. 6. Plots of the second (a) and third (b) moments of the nearest-neighbor bond length distribution of the $Ga_{1-x}In_xP$ random alloy for different compositions x. The distributions are defined as $\langle(r-R_{A\text{-}C})^2\rangle$ for the second moment and $\langle(r-R_{A\text{-}C})^3\rangle$ for the third moment, where $R_{A\text{-}C}$ is the average A-C bond length, and r's are the various bond lengths in the random alloys.

lengths in the virtual alloy of composition x, $r(x)=xr_{A\text{-}C}+(1-x)r_{B\text{-}C}$. The basic features of the results of the simulation are as follows.

(i) The distribution is bimodal, i.e., the individual identities of Ga-P and In-P are preserved in the alloy.

(ii) For In-rich alloys, the In-P bond distribution has a sharp cutoff. Conversely, for Ga-rich alloys, the Ga-P distribution has a sharp cutoff.

(iii) The Ga-P distribution is broader than the In-P distribution. This is seen more clearly by inspecting moments of the distribution, as given in Fig. 6. The Ga-P nearest-neighbor bond-length distribution [Fig. 6(a)] has a higher second moment $\langle(r-R_{A\text{-}C})^2\rangle$ than In-P. Figure 6(b) shows similar trends in the third moment $\langle(r-R_{A\text{-}C})^3\rangle$ of the nearest-neighbor bond-length distribution.

We see from Fig. 5 that our simple model (described in Appendix B; see also Fig. 7) explains the main features of the numerically simulated distribution, namely the bimodality, and the sharp cutoffs of the A-C distribution in AC-rich alloys. However, the following also hold.

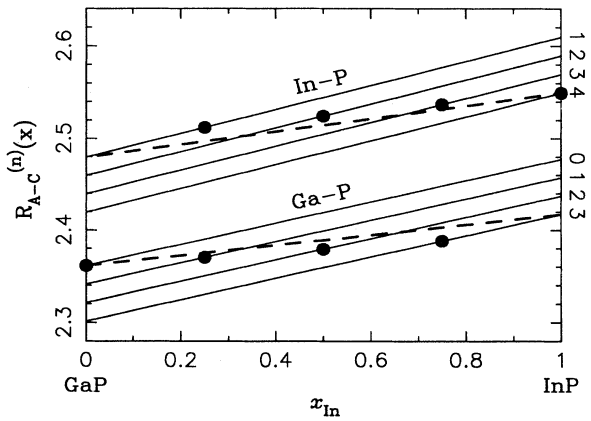

FIG. 7. Plot of the bond lengths $R_{A\text{-}C}^{(n)}(x)$ of the different clusters in the $Ga_{1-x}In_xP$ random alloy (solid lines) calculated from Eq. (B7) in Appendix B. The possible clusters are $n=0$, 1, 2, and 3 for $Ga_{4-n}P$ and $n=1$, 2, 3, and 4 for In_nP. The dashed lines denote the alloy average bond lengths $\langle R_{A\text{-}C}^{(x)}\rangle$ calculated using Eq. (B1), while the solid dots denote the bond lengths $R_{A\text{-}C}^{(n)}(X_n)$ in ordered compounds where $X_n=n/4$.

(i) The simulation produces smooth distributions while the model contains a maximum of four distinct steps (Fig. 5). Clearly, the difference between the simulation and the model reflects effects beyond nearest-neighbor bonds.

(ii) The simulation produces a wider bond distribution for Ga-P than for In-P (see Fig. 5 at $x=0.5$) while the simple model with $|K_{\text{Ga-P}}|=|K_{\text{In-P}}|$ does not. Our discussion of Sec. V A showed [Eq. (5.8)] that the effective Ga-P force constants within the ternary alloy are softer than the In-P force constants, or

$$|K_{\text{Ga-P}}| > |K_{\text{In-P}}| \ . \tag{6.1}$$

Thus our model and the occurrence of wider Ga-P bond distribution confirm the expectation of Eq. (5.8).

B. Next-nearest-neighbor distance distribution

Figure 8 depicts the next-nearest-neighbor (NNN) distance distributions for the four types of next-nearest-neighbor bonds In-In, Ga-Ga, Ga-In, and P-P, in the chemically random $Ga_{1-x}In_xP$ alloy. The dashed vertical lines denote the next-nearest-neighbor distances in the virtual alloy of composition x. We see that while first-neighbor distributions are bimodal (Fig. 5), the next-nearest-neighbor cation distributions are unimodal while the anion distribution is multimodal. The shape of the In-In, Ga-Ga, and Ga-In distance distributions are almost identical while the P-P distribution is different, exhibiting as many as five peaks. This shows clearly that the major displacements in the alloy are of the P atoms. The reason for the different behavior of cation vs anion distances is topological: The Ga and In atoms at $T=0$ remain in their lattice sites with only minor deviations. The P atoms at $T=0$ have 14 possible off-lattice locations in addition to the lattice site location (see Appendix C). This explains why the distributions of the In and Ga atoms have single peaks, while the distributions of the P atoms have many peaks.

C. Bond angle distribution

Figure 9 depicts the bond angle distributions for the random $Ga_{1-x}In_xP$ alloy at the compositions $x=0.10$, 0.25, 0.50, 0.75, and 0.90, for the three kind of bond angles: the angles around the P atoms ($\Theta_{i\text{-P-}j}$), the angles around the In atoms ($\Theta_{i\text{-In-}j}$), and the angles around the Ga atoms ($\Theta_{i\text{-Ga-}j}$). The last panel shows the total bond angle distribution ($\Theta_{i\text{-}j\text{-}k}$). Note how the high-angle ($\Theta\sim115°$) satellite at In-rich alloys becomes a low-angle ($\Theta\sim105°$) satellite as the alloys become Ga rich. This means that in In-rich alloys a significant fraction of all

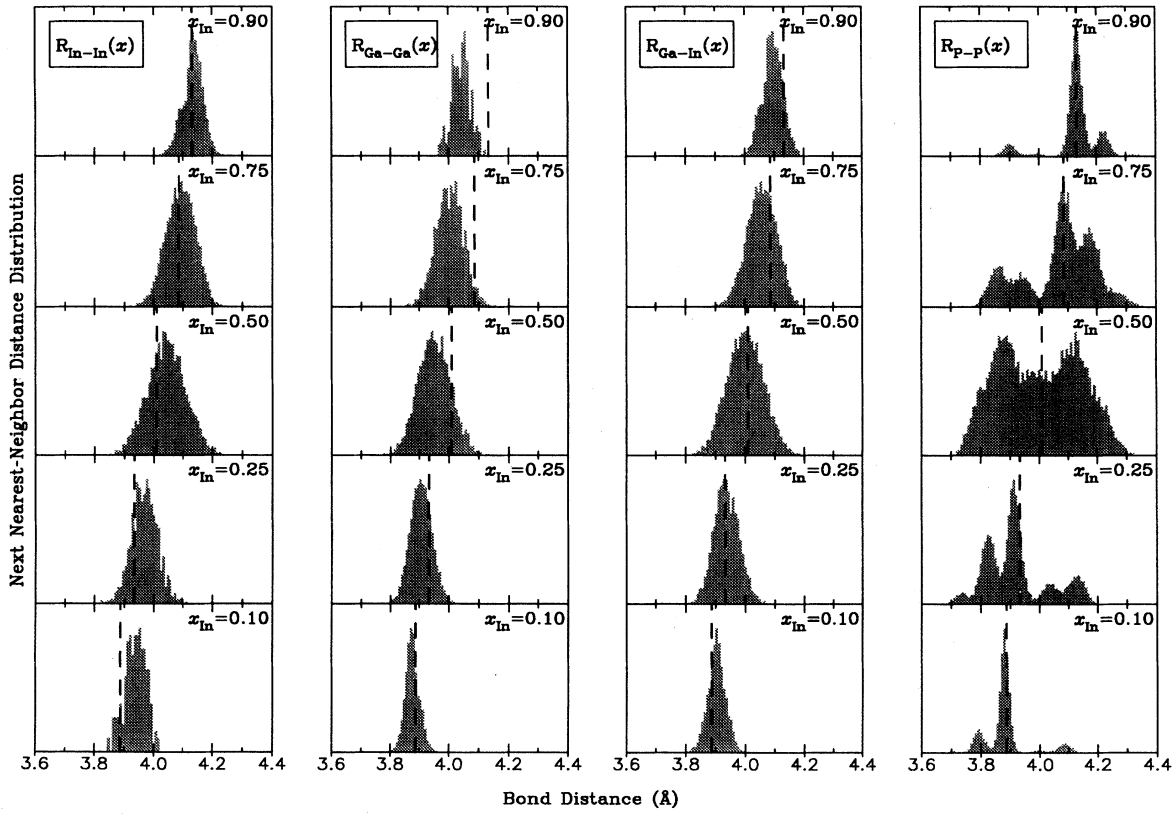

FIG. 8. Histogram plots of the next-nearest-neighbor distance distributions of the chemically random $Ga_{1-x}In_xP$ alloys for some selected compositions x. Results are given for the In-In, Ga-Ga, Ga-In, and P-P distances. The dashed vertical lines denote the next-nearest-neighbor distances in the virtual alloy of composition x.

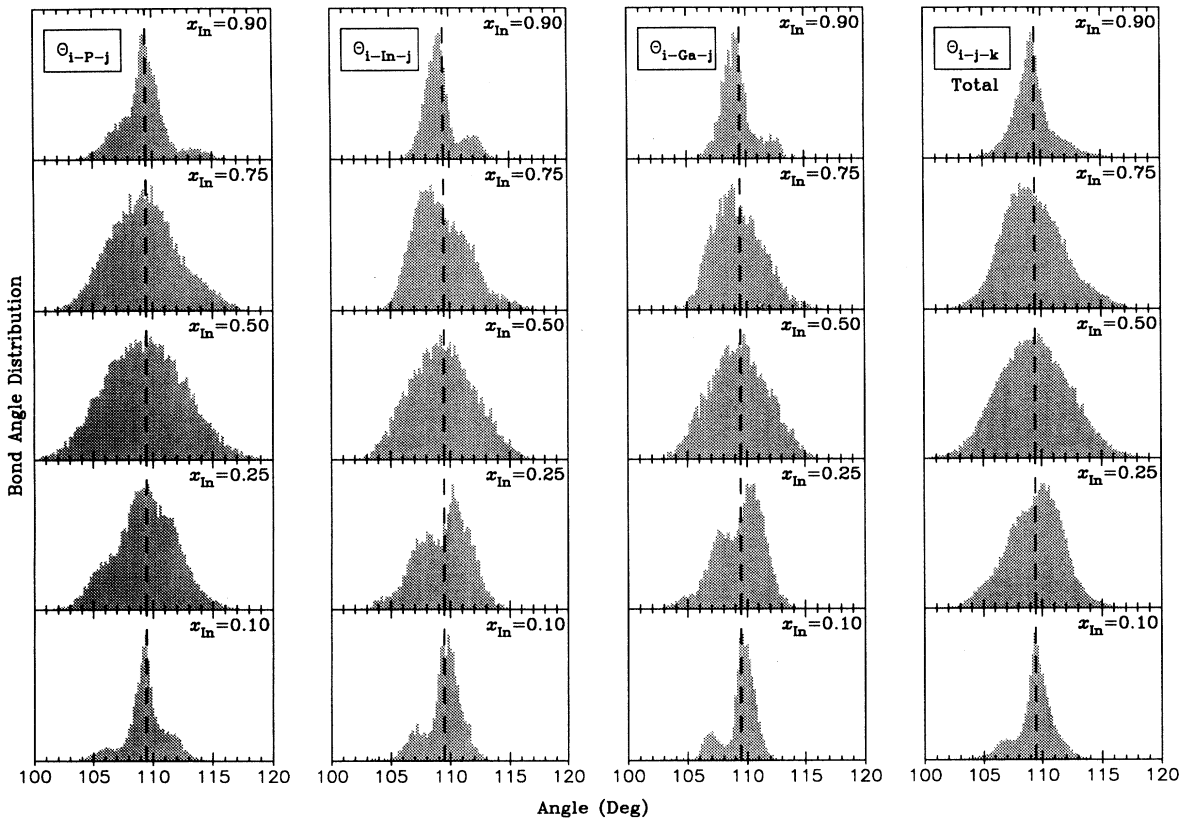

FIG. 9. Histogram plots of the bond angle distributions of the chemically random $Ga_{1-x}In_xP$ alloys for some selected compositions x. Results are given for bond angles around the P atoms ($\Theta_{i\text{-P-}j}$), the In atoms ($\Theta_{i\text{-In-}j}$), and the Ga atoms ($\Theta_{i\text{-Ga-}j}$). The total bond angle distribution is ($\Theta_{i\text{-}j\text{-}k}$). The dashed vertical lines denote the tetrahedral bond angle of the zinc-blende lattice (109.47°).

bond angles open up, while in Ga-rich alloys a significant number of bond angles close up. Our simulation further shows that the bond angles around either anions or cations are rather soft, exhibiting significant deviations from the tetrahedral values. In contrast, as Fig. 4 shows, the nearest-neighbor bond lengths are rather rigid, being close to the ideal values in the binary constituents.

D. Pair-correlation function

Figure 10 describes the pair-correlation function of chemically random $Ga_{1-x}In_xP$ alloys for various compositions. The pair-correlation function $R(r)$ is the average radial atomic density $\rho(r)$ in the interval between r and $r+\Delta r$, where r is the bond length and Δr is the width of the histogram

$$R(r)=\int_r^{r+\Delta r}\rho(r)dr \ . \tag{6.2}$$

The pair-correlation function is plotted in Fig. 10 for $r>2$ Å, as there are no bonds shorter than 2 Å. The first peak represents the first shell (nearest neighbors) bond length, the second represents the second shell, etc. The dashed lines denote the bond lengths in the virtual alloy of composition x. For comparison, we also give results for pure GaP and pure InP ($x=0$ and 1). For these pure compounds, the pair correlations exhibit sharp peaks as all bond lengths and bond angles are equal. In the first alloy shell ($s=1$), the peak of the GaP and InP is split into two subpeaks. The left subpeak represents the shorter Ga-P bond and the right subpeak represents the longer In-P bond. (This can be seen more clearly in the nearest-neighbor distance distribution in Fig. 5.) From the second shell on ($s\geq 2$), the peaks of the alloy are broadened as the alloy is formed. The centers of the peaks $\langle r(x)\rangle_s$ are located in the virtual lattice

$$\langle r(x)\rangle_s = x r_{s,A\text{-}C}+(1-x)r_{s,B\text{-}C} \ , \tag{6.3}$$

shown in Fig. 10 as dashed vertical lines. Figure 10 demonstrates that, in substitutional random alloys, the overall long-range order of the underlying lattice is preserved.

E. $T=0$ phosphorus displacements in the random alloy

Figure 11 shows contour plots of the P-atom displacements of numerical simulated random $Ga_{1-x}In_xP$ alloys for three different compositions, $x=0.25$, 0.5, and 0.75 (left panels). The right-hand panels show similar plots of the P-atom displacements predicted by the model described in Appendix C and Fig. 11. The three-dimensional displacements are projected onto the three principal planes (100), (110), and (111). Each plot represents the P-atom displacements, averaged over some 200 samples which were relaxed at $T=0$. The contours

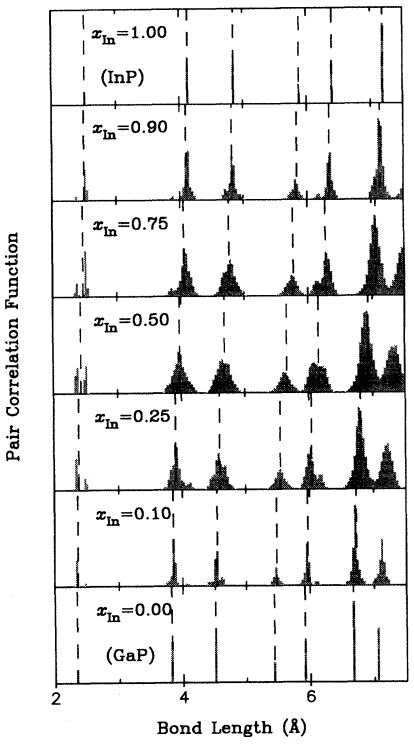

FIG. 10. The pair-correlation function of the $Ga_{1-x}In_xP$ random alloys for five different compositions $x=0.10$, 0.25, 0.50, 0.75, and 0.90, and for the two binary compounds GaP ($x=0$) and InP ($x=1$). The distributions extend up to the sixth-nearest neighbor.

represent different probabilities of finding the P atom. The length of the squares in the plots is 0.5 Å.

As explained in Appendix C, there are 14 off-lattice locations in addition to the zinc-blende lattice site location for the P atom: eight in the (111) bond directions and six between two adjacent bond directions. These sites cannot be observed simultaneously in a single projection plot since overlaps appear in the two-dimensional representations. For example, in the (100) projections for $x=0.5$ (shown also in a three-dimensional representation in Fig. 13) we see a single nondisplaced site which has the largest probability, and eight displaced sites: four in the (111) directions, and four in the (100) directions. The two extra (100) sites in the plane perpendicular to the projection plane are projected onto the central nondisplaced site, while each of the (111) displaced sites is a projection of two overlapping (111) sites. Only nine different sites can thus be observed in the (110) and (111) projections [Figs. 11(b) and 11(c), respectively]. Note that, in all projections, the most probable location is in the middle (e.g., the central peak in Fig. 13).

We see that despite the fact that the lattice sites were initially occupied by Ga and In in a random manner, the relaxation process has led to a deterministic pattern of atomic displacements: while the undisplaced Ga, In, and P sites have the highest probability (giving rise in reciprocal space to the usual Bragg diffraction peaks), there are several distinct high-symmetry sites with significant probability peaks. These displacements (of the order of ~ 0.1 Å) are highly correlated, and occur at specific positions at all compositions. As suggested by Glas and coworkers,[69,8] they could lead in reciprocal space to the dis-

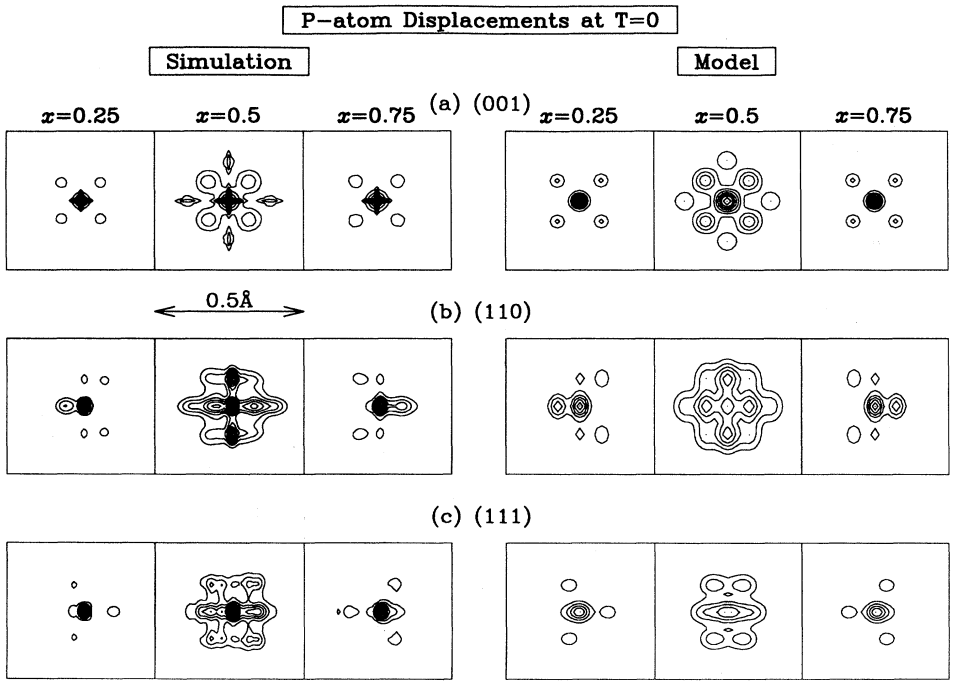

FIG. 11. Contour plots of the P-atom displacements in chemically random $Ga_{1-x}In_xP$ alloy. The displacements are represented in three projections (100), (110), and (111), for three different compositions $x=0.25$, 0.5, and 0.75. The left-hand side describes results from numerical simulations of samples relaxed at $T=0$, while the right-hand side columns are the results of our model described in Appendix C. The length of the squares in the plots are 0.5 Å.

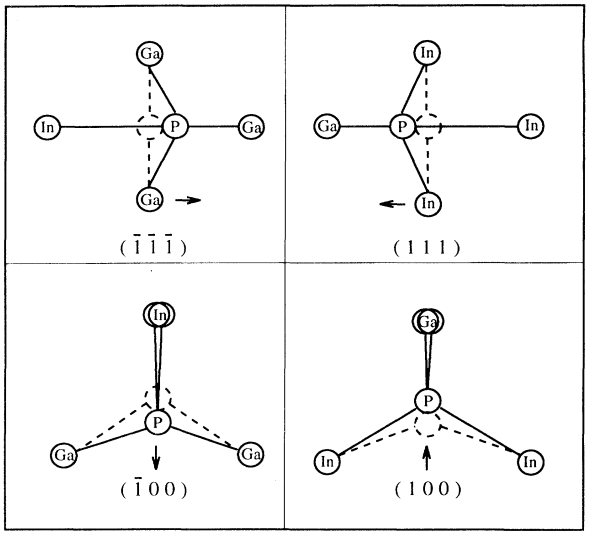

FIG. 12. Schematic diagram of four possible displacements of the P atom in the random $Ga_{1-x}In_xP$ alloy resulting from its nearest-neighbor atomic configuration.

tinct diffraction pattern observed[70] in nominally random bulk alloys.

VII. TEMPERATURE EFFECTS ON THE ATOMIC GEOMETRY

A. Static temperature smearing of displacement maps

Figure 14 shows contour plots of atomic displacements of the anions and cations in simulated samples of $Ga_{0.5}In_{0.5}P$ in three different planes and at three different temperatures. The plots represent the results of average statistics on some 200 random $Ga_{0.5}In_{0.5}P$ samples which were equilibrated at three different temperatures 40, 120, and 300 K using a MC equilibration process without spin flip. The projections were calculated with the same method used for the calculations of the projections at

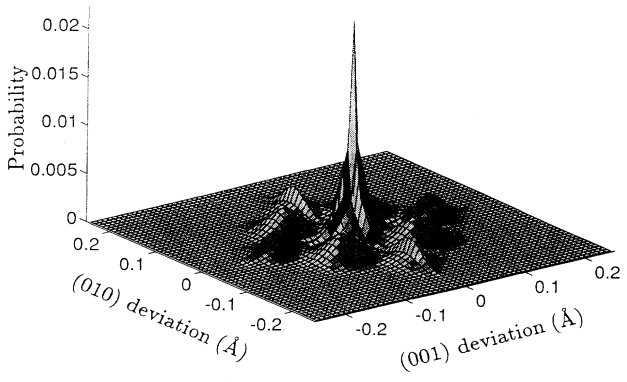

FIG. 13. Three-dimensional plot of the average possibility of the P-atom displacements in chemically random $Ga_{0.5}In_{0.5}P$ alloy at $T=0$. The plot represents the (100) plane projection of the P-atom displacements.

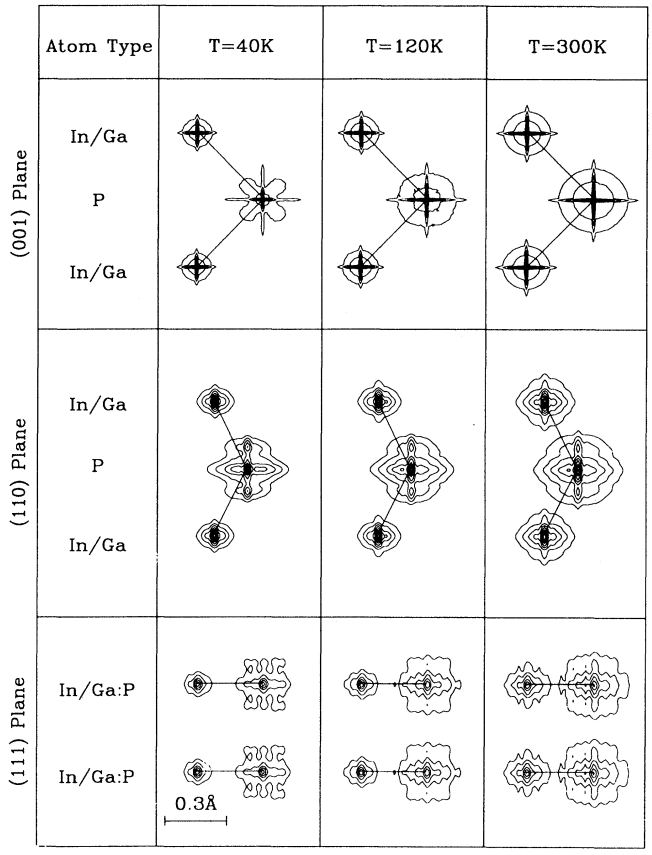

FIG. 14. Contour plots of the average atomic displacements in a random $Ga_{0.5}In_{0.5}P$ alloy projected onto the (100), (110), and (111) planes. The plots represent displacements in samples which were equilibrated at three different temperatures. In each column, the contour plots were placed in an order which represents the nearest-neighbor configuration of the plane. The marks of 0.3 Å represents the scaling of the contour plots' atomic displacements, but not the distances between the centers of the plots.

$T=0$ (Fig. 11). In Fig. 14 we show contour plots of both anions and cations. As the displacements of the In and Ga atoms are very similar, the cations contours show only the Ga displacements. The contours were placed in an order which represents the nearest-neighbor configuration of the crystallographic planes, though not drawn to scale.

The results show that (i) the anions P are displaced considerably more than the cations Ga and In. The displacements of the anions include the displaced sites which were observed at $T=0$ (Fig. 11), while the displacements of the cations are mostly thermal vibrations around the zinc-blende virtual lattice sites (compare the cations displacement maps at different temperatures in Fig. 14). (ii) The main off-center locations of the P atoms are in the six (001) directions [(100), ($\bar{1}$00), (010), (0$\bar{1}$0), (001), and (00$\bar{1}$)] (see Fig. 13). (iii) Atomic displacements in the (100) and (110) planes are considerably more directional than in the (111) plane. (iv) As the temperature is increased above $T=0$, the sharp features of the displace-

ment maps are rapidly broadened, suggesting the dominance of dynamic over static effects already at $T=120$ K. (v) Temperature broadens the anion displacement map much more in the (110) and (111) planes than in the (100) plane. This is because the (001) off-center locations of the P atoms [which are projected more clearly in the (001) maps] are more dominant than the (111) off-center locations [which are projected more clearly in the (110) and (111) maps]. (vi) As the temperature is increased, the probability of finding P atoms in the elastically hard (111) off-center locations decreases, while the probability of finding them in the elastically soft (100) locations increases.

B. Molecular-dynamics average root-mean-square thermal displacements

To calculate the time-averaged probability of the atomic displacements we apply a molecular-dynamics (MD) algorithm to our T-VFF potential. Monte Carlo algorithms cannot predict dynamic displacements as they give the maximum probability at the bottom of the potential surface (see Fig. 14). As is the case for the classic pendulum, the position probability has a minimum at the bottom of the potential surface, a result which can be obtained using a molecular-dynamics algorithm.

$Ga_{1-x}In_xP$ samples of 512 atoms were used in the calculations, and the initial In/Ga substitution was chosen randomly according to the required composition. Then a MC algorithm was applied to equilibrate the samples at a temperature $T=300$ K using the T-VFF potential. The spatial derivatives of the T-VFF potential were used for the forces in the Newtonian equations of motion of the atoms. Using these equations, the time evolution of the atomic coordinates were calculated using the Gear algorithm.[71] 500 MD cycles were used for the initial equilibration, and then the average displacements of the atoms were calculated for 2400 additional MD cycles. The rms average displacements defined as

$$\langle \Delta U \rangle_j = \left[\frac{\sum_{i=1}^{n} [\bar{U}_j - U_j(t_i)]^2}{n} \right]^{1/2} , \tag{7.1}$$

were calculated separately for each atom in the sample. Here $U_j(t_i)$ is the position of atom j at the instant $t_i=i\Delta t$, Δt is the interval between samplings, and $\bar{U}_j$ is the time-averaged position of atom j given by $\bar{U}_j=1/n\sum_{i=1}^{n}U_j(t_i)$. The above algorithm was applied to 100 different initial random atomic configurations, and the average rms displacements for each species α were calculated. The MD results are shown in Fig. 15. We observe the following.

(i) In the pure GaP and InP binaries the anions and cations have similar mean-square dynamic displacements (MSDD's). This agrees with the suggestions of Garbulsky and Ceder,[72] who showed that the leading term of the vibrational effective cluster interaction (VECI) at high temperatures is independent of the masses of the atoms, and only the spring constants are involved. On the other hand, is most II-VI semiconductors there is a major

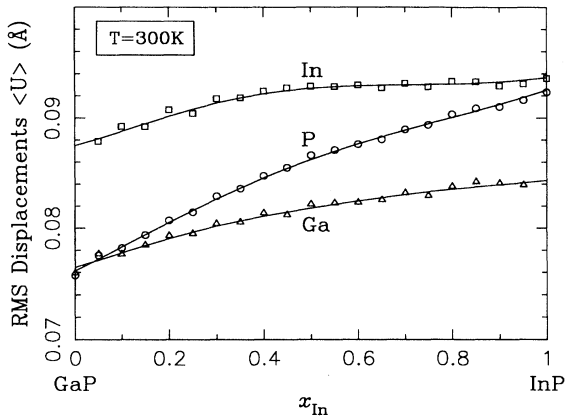

FIG. 15. Molecular-dynamics results of the total root-mean-square (rms) displacements $\langle U \rangle$ of the In (squares), Ga (triangles), and P (circles) atoms in the random $Ga_{1-x}In_xP$ alloy at a temperature $T=300$ K vs In composition x_{In}. The solid lines are interpolations of the calculated results.

difference between the MSDD of the anions and cations.[73] This can be understood by the weaker bonds in the II-VI semiconductors as compared to the III-V's. As a result of the weak spring constants in the II-VI's, the leading term of the VECI is expected to be less dominant, and hence the second term, involving the masses of the atoms will be more effective.

(ii) The cation MSDD increases monotonically with In composition. This can be explained as follows: We saw in Fig. 4 that the Ga-P bond length in In-rich alloys is shorter than the same bond in pure GaP, i.e.,

$$R_{\text{Ga-P}}(\text{InP:Ga}) > R_{\text{Ga-P}}(\text{GaP}) ,$$

and, conversely,

$$R_{\text{In-P}}(\text{GaP:In}) < R_{\text{In-P}}(\text{InP}) , \tag{7.2}$$

where InP:Ga and GaP:In represent In- and Ga-rich $Ga_{1-x}In_xP$ alloys, respectively. Thus, in the alloy environment, the shorter of the two bonds (Ga-P) elongates, while the longer of the two (In-P) shortens. Since vibrational frequencies decrease with bond elongation, the above implies

$$\begin{aligned} &\omega_{\text{Ga-P}}(\text{InP:Ga}) < \omega_{\text{Ga-P}}(\text{GaP}) , \\ &\omega_{\text{In-P}}(\text{GaP:In}) > \omega_{\text{In-P}}(\text{InP}) . \end{aligned} \tag{7.3}$$

This means that (a) bond relaxation reduces the frequency difference $\omega_{\text{In-P}}-\omega_{\text{Ga-P}}$ in the alloy relative to the pure binaries, and that (b) the vibrational frequency of the atoms in the dilute alloys (e.g., the Ga-P mode in In-rich alloys) is close to the vibrational frequency of the atoms in the pure complementary compound (here pure GaP). This is indeed observed by Raman experiments.[74] The MSDD scales inversely with frequencies, thus

$$\begin{aligned} &U_{\text{Ga}}(\text{InP:Ga}) > U_{\text{Ga}}(\text{GaP}) , \\ &U_{\text{In}}(\text{GaP:In}) < U_{\text{In}}(\text{InP}) . \end{aligned} \tag{7.4}$$

Here we denote $U_\alpha \equiv \langle U_\alpha \rangle$, the average rms displace-

ments for the species α. As seen in Fig. 15, this explains why both U_{Ga} and U_{In} increase in In-rich alloys. Note that the composition dependence in Fig. 15 is monotonic; no evidence of a drop in U is found at any intermediate composition similar to that found in some II-VI ternaries.[75,77]

(iii) While the static displacement maps (Fig. 11) show that the anion has a larger probability than the cation to reside at off-center positions, the dynamic displacements (Fig. 15) show $U_{In} > U_P > U_{Ga}$. In fact, the anion MSDD changes monotonically with composition from $U_P \sim U_{Ga}$ in pure GaP, to $U_P \sim U_{In}$ in pure InP. The different peaks of the anion in the static displacement map (Fig. 11) are related to the different anion off-site locations in the five different clusters $Ga_{1-n}In_nP$ for $n=0$, 1, 2, 3, or 4. One may expect different vibrational modes (and possibly different vibration amplitudes) for different clusters, but these cannot be observed in the MSDD representation, as the probability of the different clusters is monotonic with x (see Appendix B).

C. Short-range order

Cowley's short-range order (SRO) parameter is given by[79]

$$\alpha_{A\text{-}B}=1-\frac{P^{A/B}}{x_B}\ , \tag{7.5}$$

where $P^{A/B}$ is the probability that an atom A has a B next-nearest neighbor, and x_B is the composition of the B atoms. For a random alloy, $\alpha_{A\text{-}B}=0$. For $A\neq B$, $\alpha_{A\text{-}B}<0$ denotes the association of unlike atoms (anticlustering), while $\alpha_{A\text{-}B}>0$ denotes the association of like atoms (clustering). Equation (7.5) gives $\alpha_{Ga\text{-}In}=\alpha_{In\text{-}Ga}$, and for $x=0.5\alpha_{Ga\text{-}Ga}=\alpha_{In\text{-}In}$ and $\alpha_{Ga\text{-}Ga}=1-\alpha_{Ga\text{-}In}$.

Figure 16 depicts the calculated short-range order parameter for the next-nearest-neighbor shell, i.e., the cations of the mixed fcc sublattice. Each point is an average over some 200 $Ga_{0.5}In_{0.5}P$ simulated samples equilibrated at a temperature T. The MC equilibration process [Eqs. (4.2) and (4.3)] included spin flips as well as atomic coordinate and volume relaxations. A uniform composition in the range of temperatures was achieved by adjusting the value of the chemical potential difference $\Delta\mu=\mu_{Ga}-\mu_{In}$ during the calculations to obtain the required composition. This is essential as the SRO parameter is a function of composition as well as temperature.

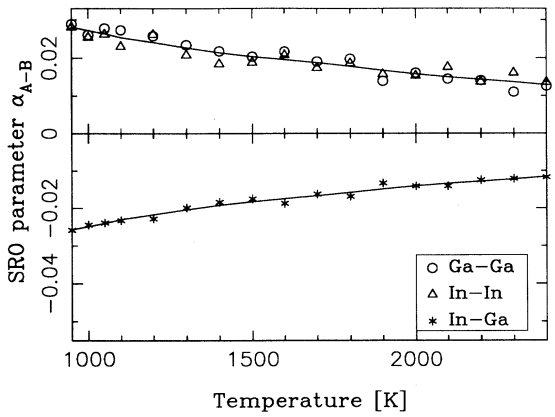

FIG. 16. Cowley's short-range order parameter [Eq. (7.5)] for the next-nearest-neighbor mixed cation shell of $Ga_{0.5}In_{0.5}P$ at different temperatures above the miscibility-gap temperature. The results are averages on $Ga_{0.5}In_{0.5}P$ simulated samples equilibrated at temperature T. The MC equilibration process included spin flip as well as atomic coordinates and volume relaxations.

At high temperature $\alpha_{A\text{-}B}\to 0$, indicating that the alloy becomes chemically random. Below the miscibility gap temperature T_{MG}, there is a phase separation into the two basic phases, i.e., the In-rich and Ga-rich phases, and therefore the sample contains islands of InP and GaP clusters. We see in Fig. 16 that even for T far above the miscibility gap temperature $T_{MG}=870$ K, there is still considerable SRO in the form of anticlustering. Since for $x=0.5$ we have, from Eq. (7.5), $P^{Ga/In}=0.5-0.5\alpha_{Ga\text{-}In}$, then $\alpha_{Ga\text{-}In}<0$ in Fig. 16 means that the mixed cation exists with a higher probability than what random statistics will grant (anticlustering). Note also that for $x=0.5$ we have $P^{Ga/Ga}=P^{In/In}=1-P^{Ga/In}$, so the above conclusion implies that Ga-Ga and In-In exist with a lower probability than that given by random statistics. For example $\alpha_{Ga\text{-}Ga}(1500\text{ K})\sim 0.02$ means that the Ga-Ga pair concentration is 2% less than that given by random statistics. The anticlustering behavior we observed in our model is in agreement with the results of the ε-G approach described in Sec. IV B of Ref. 51.

D. Comparison of displacements with experiment

The average bond distances (Fig. 4) which are amenable to EXAFS measurements do not reveal the actual spatial distribution of the atoms in the alloy. In fact, if an atom of type α(=P,Ga,In) can have a series of displaced sites $\mathbf{R}_i^{(\alpha)}(x)$ with probability $P_i^{(\alpha)}(x)$, the EXAFS measurement (and our calculation in Fig. 4) would provide the average $\mathbf{R}^{(\alpha-\beta)}(x)=\sum_{ij}P_i^{(\alpha)}(x)P_j^{(\beta)}(x)|R_i^{(\alpha)}(x)-R_j^{(\beta)}|$ of the distribution and its width. Our calculation permits us, however, to take a step backwards and to focus on the probability of finding an atom of type α in a given position on a crystalline plane.

As far as we know, no direct experimental results are available for the rms displacements in $Ga_{1-x}In_xP$, so only comparisons with related systems are possible. Ion-channeling measurements are in principle capable of detecting small displacements of atoms from their ideal lattice sites.[80] They are therefore ideal to probe experimentally the atomic geometries predicted here. Haga *et al.*[76] in 1985 observed abnormal dechanneling in $Ga_{0.47}In_{0.53}As$ which they attributed to small atomic displacements in the ternary alloy, though they were unable to pin down the particular atom which may be displaced. A lattice average rms displacement obtained in that work was $U=0.07$ Å, a result which is very close to our predictions (Fig. 15). This observation, although found in a different III-V alloy, may well be due to anion displacements similar to those predicted in the present work for

$Ga_{1-x}In_xP$. More recently, a method which combines Rutherford backscattering (RBS) and particle-induced x-ray emission (PIXE) with channeling has been developed.[81] This method allows a determination of the location in the lattice of each atomic species contained in a mixed crystal. It has recently been applied to II-VI mixed crystals, i.e., $Zn_xCd_{1-x}Te$ (for a range of x values) and to a lesser extent to $Hg_xCd_{1-x}Te$.[77] The results for $Zn_xCd_{1-x}Te$ indicate that in order to best fit the experimental data, a permanent displacement of the Te atom by about 0.12 Å (for $x=0.1$) toward the shorter Zn-Te bond is required. The fact that the mixed (A,B) cation sublattice is hardly affected by the ternary mixture, while the common anion C (Te in the above case) undergoes substantial displacements, is in accord with the results of the present calculations for $Ga_{1-x}In_xP$ which predict the common anion (P) to show a multimodal distribution which depends on crystal composition x (see Figs. 5 and 8). The expected deviations for P in $Ga_{1-x}In_xP$ are of the order of 0.1 Å, similar to those found experimentally for $Zn_xCd_{1-x}Te$. The channeling experiments, when carried out at different temperatures, are also sensitive to the vibration of the atoms around their equilibrium positions. These were found in Ref. 77 to vary with x for both $Zn_xCd_{1-x}Te$ and $Hg_xCd_{1-x}Te$ in a nonmonotonic way, exhibiting minima for particular alloy compositions ($x\approx0.1$ for $Zn_xCd_{1-x}Te$ and $x\approx0.3$ for $Hg_xCd_{1-x}Te$ (i.e., at $y=0.7$ for $Hg_{1-y}Cd_yTe$). Such bowing was not observed in our MD calculations for the $Ga_{1-x}In_xP$ alloy.

By using the standard VFF potentials[52,53] for ZnTe and CdTe, we have calculated the average rms displacements $\langle U_\alpha \rangle$ for Zn, Cd, and Te in the binaries ZnTe and CdTe in the same way as done here for $Ga_{1-x}In_xP$ (Fig. 15). We could reproduce the observed trend in the relations between the anion and cation rms displacements rather well.[78] However, no evidence was found for the anomalous, nonmonotonic u vs x inferred in Ref. 77. The latter results thus remain unexplained in terms of our theory of homogeneous alloys.

VIII. SUMMARY

We have developed a method to adopt the elastic valence-force-field interatomic potentials of binary compounds to the ternary mixture of the two binaries. Three parameters were added to the VFF potential functions, and their values were calculated using a simulated annealing algorithm to best fit the excess energies of ordered structures determined by first-principles local-density calculations. This method was applied to the calculation of the $Ga_{1-x}In_xP$ interatomic potentials.

Using our ternary valence-force-field potentials in Monte Carlo calculations, we found good agreement with measured mixing enthalpy, nearest-neighbor bond lengths, and temperature-composition phase diagrams.

In simulated $Ga_{1-x}In_xP$ random alloys, major off-site displacements of the P atom were observed. These displacements are affected mostly by the P atoms nearest-neighbor configuration. We provided a nearest-neighbor model which predicts these displacements. The observed P-atom displacements are of the order of ~0.1 Å, and are therefore measurable.

Molecular-dynamics calculations showed similar mean-square dynamic displacements for the anions and cations in the pure GaP and InP binaries. In the $Ga_{1-x}In_xP$ random alloy, we observed a monotonic increase of the MSDD's of the cations as well as the anions with In composition.

ACKNOWLEDGMENTS

A.S. would like to thank the National Renewable Energy Laboratory for its hospitality during a visit in which part of this work was done. Work at the Technion was supported by the U.S.–Israel Binational Science Foundation under Grant No. 88-00295. We also acknowledgment partial support from the Technion Institute for Theoretical Physics and the hospitality of the Physics Department and the Solid State Institute of the Technion. The work at NREL was supported by U.S. DOE Contract No. DE-AC02-83-CH10093. We thank the Laboratory for Parallel Computing Research in the Technion for an allocation of time on the Meiko computer. The authors are grateful to Dr. S.-H. Wei for providing the LAPW results and for many useful discussions and advice, and to Dr. C. Wolverton for comments on the manuscript. We thank Dr. K. E. Khor for discussions of his potential function and Dr. J. Tersoff for discussions of his method of phase-diagram calculations.

APPENDIX A: COMPARISON OF THE VFF WITH OTHER POTENTIALS

We have compared our excess energies in Tables I and II to those obtained with the KDS potential.[49] Specifically, we use Eqs. (1)–(3) in Ref. 49, fixing the coordination number $Z\equiv4$. The results for the 25 ordered structures are shown in Tables I and II. They exhibit large deviations from the LDA data. Das Sarma and Khor have calculated the excess energy of the $GaInP_2$ CA structure (defined in Table I here and in Ref. 55) to be 128.04 meV/four atoms, compared to our value of 83.8 meV/four atoms using the same potential. The difference probably reflects a more refined structural optimization in the current work. We have thus attempted to modify the KDS potential to systematically improve the agreement with the LDA. We cite the modified (M) potential M-KDS using the notation

$$E_{\rm config}(\sigma)=\tfrac{1}{2}\sum_{l}\sum_{s=1}^{2}\sum_{m=1}^{4}Ae^{-\beta(r_{lsm}-R_{ls})^{\gamma}}\times\left[e^{-\theta r_{lsm}}-\frac{B_0e^{-\lambda r_{lsm}}}{Z_{ls}^{\alpha}}\right]G(\theta)\ . \tag{A1}$$

Here the interatomic distance is

$$r_{lsm}=\mathbf{r}_m(l,s)\cdot\mathbf{r}_m(l,s)\ , \tag{A2}$$

and the minimum interatomic distance between the nearest neighbors is

$$R_{ls}=\min_m|r_m(l,s)|\ . \tag{A3}$$

The three-body term is

$$G(\theta)=1+\sum_{n\neq m,n=1}^{4}\cos(\eta\Delta\theta_{lsmn}-1)\ , \tag{A4}$$

where

$$\Delta\theta_{lsmn}=|\theta_{lsmn}-\theta_i|\ , \tag{A5}$$

and the bond angle is

$$\theta_{lsmn}=\cos^{-1}\frac{\mathbf{r}_m(l,s)\cdot\mathbf{r}_n(l,s)}{|r_m(l,s)|\cdot|r_n(l,s)|}\ . \tag{A6}$$

$\mathbf{r}_m(l,s)$ is the vector connecting atom s in unit cell l to its mth nearest neighbor, Z_{ls} is the effective coordination number of atom s in unit cell l. A, B_0, θ, λ, α, β, and γ are adjustable parameters. We used the original KDS parameters for In-P and Ga-P. However, unlike the original form of KDS, we moved the $G(\theta)$ term outside the brackets of the $E_{\text{config}}(\sigma)$ expression. This form is similar to the improved version of the KDS potential for Si-Ge interactions.[59] We omitted the sine term in the $G(\theta)$ expression,[60] and fixed the effective coordination number $Z_{ls}\equiv 4$ (since if we let Z_{ls} be calculated from the formula of KDS, the excess energy of some of the ordered structures became negative, a totally unphysical result).

The results of the excess energies as obtained by the LDA, the original VFF, the ternary T-VFF, and the modified KDS (M-KDS) potentials are summarized in Tables I and II. The original VFF values were calculated using the Keating VFF parameters[52] [Eq. (4.4)], with the Martin assumptions for the ternary interaction parameters[53] [Eq. (4.7)]. Even with the improved form, the M-KDS formation enthalpies show large deviations from the *ab initio* LDA results. For example, the M-KDS formation enthalpies of the [111]-oriented superlattices are about the same as those of the [001]-oriented superlattices, while *ab initio* calculations show that the formation enthalpies of the [111]-oriented superlattices are about 50% higher than those of the [001]-oriented superlattices. Since the differences between the superlattices are in the three-body interaction, we tried to vary the bond-bending parameters n_{InP} and η_{GaP} of the KDS potential in order to better fit its energy surface to the *ab initio* calculations. We found that major changes are required in order to attain better fits to ternary compounds. However, within these changes the potential no longer correctly predicts the elastic coefficients of the InP and GaP binary compounds. We were unable to significantly improve the agreement between the KDS potential and the LDA results. In what follows, we thus use only the T-VFF.

APPENDIX B: A MODEL FOR THE NEAREST-NEIGHBOR BOND-LENGTH DISTRIBUTION

We explain the features of the simulated nearest-neighbor bond-length distribution in terms of a simple model. We will distinguish the average alloy bond lengths $\langle R_{\text{Ga-P}}(x)\rangle$ and $\langle R_{\text{In-P}}(x)\rangle$ from the bond lengths $R^{(n)}_{\text{Ga-P}}(x)$ and $R^{(n)}_{\text{In-P}}(x)$ of the individual, P-centered $Ga_{4-n}In_n$ clusters ($0\le n\le 4$). From Eq. (2.3b) we see that the alloy-averaged nearest-neighbor bond lengths depend on the cluster bond lengths of all 2^N configurations. To capture the essential physics, however, we will consider four simplifying assumptions: (a) The alloy-averaged bond lengths are linear function of composition (Fig. 4). That is,

$$\begin{aligned}\langle R_{\text{Ga-P}}(x)\rangle&=R^0_{\text{Ga-P}}+x\Delta_{\text{GaP}}\ ,\\ \langle R_{\text{In-P}}(x)\rangle&=R^0_{\text{In-P}}+x\Delta_{\text{InP}}\ .\end{aligned} \tag{B1}$$

Here R^0_{AC} are the bonds in the pure AC compounds, and Δ_{AC} in the slope of the dashed lines in Fig. 4 given by Eq. (5.11). (b) The alloy-averaged bond length depends only on the nearest-neighbor clusters, i.e., on the five $Ga_{4-n}In_n$ tetrahedra. (c) The probability of finding a cluster n at a composition x is given by the random (Bernoulli) formula

$$P^{(n)}(x)=\binom{4}{n}x^n(1-x)^{4-n}\ . \tag{B2}$$

(d) The mixed (cation) sublattice does not relax from the ideal fcc positions. The relaxation thus occurs only by the common sublattice C.

The remaining missing element of our model is to find how the individual cluster bond lengths $R^{(n)}_{\text{Ga-P}}(x)$ and $R^{(n)}_{\text{In-P}}(x)$ depend on n and x. This can be argued as follows, using $x=\frac{1}{2}$ as an example. For the $n=2$ cluster Ga_2In_2, it makes sense to assume that

$$\begin{aligned}R^{(2)}_{\text{Ga-P}}(x=\tfrac{1}{2})&=\langle R_{\text{Ga-P}}(x=\tfrac{1}{2})\rangle\ ,\\ R^{(2)}_{\text{In-P}}(x=\tfrac{1}{2})&=\langle R_{\text{In-P}}(x=\tfrac{1}{2})\rangle\ ,\end{aligned} \tag{B3}$$

i.e., that the $n=2$ cluster bond lengths are equal to the average alloy bond lengths at $x=\frac{1}{2}$. However, the Ga-P bond appears also in the clusters $n=0$, 1, and 3. In the cluster $GaIn_3$, the three In-P bonds push the single Ga-P bond, therefore its length is shorter than its length in the Ga_2In_2 cluster $R^{(3)}_{\text{Ga-P}}(0.5)<R^{(2)}_{\text{Ga-P}}(0.5)$. In the cluster Ga_3In, the three Ga-P bonds pull the single In-P bond, therefore the three Ga-P bonds are longer than their length in the Ga_2In_2 cluster $R^{(1)}_{\text{Ga-P}}(0.5)>R^{(2)}_{\text{Ga-P}}(0.5)$. In the Ga_4 cluster there are four Ga-P bonds, therefore their length is longer than in the Ga_3In cluster $R^{(0)}_{\text{Ga-P}}(0.5)>R^{(1)}_{\text{Ga-P}}(0.5)$. These arguments suggest that

$$R^{(0)}_{\text{Ga-P}}(x)>R^{(1)}_{\text{Ga-P}}(x)>R^{(2)}_{\text{Ga-P}}(x)>R^{(3)}_{\text{Ga-P}}(x)\ , \tag{B4}$$

and the opposite is true for the In-P bond length, namely

$$R^{(1)}_{\text{In-P}}(x)<R^{(2)}_{\text{In-P}}(x)<R^{(3)}_{\text{In-P}}(x)<R^{(4)}_{\text{In-P}}(x)\ . \tag{B5}$$

These relationships can be represented by a simple linear formula

$$\begin{aligned}R^{(n)}_{\text{Ga-P}}(x)&=\langle R_{\text{Ga-P}}(x)\rangle+(4x-n)K_{\text{GaP}}\ ,\\ R^{(n)}_{\text{In-P}}(x)&=\langle R_{\text{In-P}}(x)\rangle+(4x-n)K_{\text{InP}}\ ,\end{aligned} \tag{B6}$$

where K_{AC} is a displacement for the AC sublattice. Figure 7 depicts these relationships schematically. Note that Baldereschi and Peressi[82] have not distinguished the bond lengths $R^{(n)}$ in ordered compounds (solid dots in Fig. 7) from the alloy values $\langle R(x)\rangle$ (dashed lines in Fig. 7); i.e.,

they use $K_{GaP}=K_{InP}=0$ in Eq. (B6).

Substituting Eq. (B1) into (B6) gives

$$R^{(n)}_{Ga\text{-}P}(x)=R^{0}_{Ga\text{-}P}+(4K_{GaP}+\Delta_{GaP})x-nK_{GaP}\ ,$$
$$R^{(n)}_{In\text{-}P}(x)=R^{0}_{In\text{-}P}+(4K_{InP}+\Delta_{InP})x-nK_{InP}\ . \tag{B7}$$

The solid lines in Fig. 5 depict the histogram of $P^{(n)}(x)$ vs $R_{A\text{-}C}(x)$ using Eqs. (B2) and (B7), and the numerical values

$$\Delta_{GaP}=0.036\ \text{Å}\ ,$$
$$\Delta_{InP}=0.050\ \text{Å} \tag{B8}$$

from our calculation of Table IV, and

$$K_{GaP}=-K_{InP}=0.02\ \text{Å}\ , \tag{B9}$$

fit to the width of the histograms of the MC results.

APPENDIX C: A MODEL FOR THE DISPLACEMENTS OF THE P ATOM

To understand the essential features of Fig. 11 we consider a model which assumes that the displacements of the P atoms reflect the properties of its four nearest bonds in the five different $Ga_{4-n}In_nP$ clusters. The mixed (cation) sublattice is assumed to be unrelaxed with respect to the ideal fcc positions. Specifically, the model assumes the following.

(i) In the $n=0$ and 4 clusters, the four bonds connecting the P atom are equal, so the P atom is located in the tetrahedron center.

(ii) In the $n=1$ cluster there is one long In-P bond and three short Ga-P bonds, so the P atom is displaced away from the longer In-P bond, in one of the four (111), $(\bar{1}11)$, $(1\bar{1}\,\bar{1})$, or $(\bar{1}1\bar{1})$ directions (according to the In-P bond direction). Since the random alloy is homogeneous and isotropic, all of these directions have an equal probability. In the $n=3$ cluster, there is one short Ga-P bond and three long In-P bonds, so the equilibrium locations of the P atom are in opposite direction relative to the $n=1$ cluster. Let δ_n denote the displacement amplitude of the P atom along the bond direction in the cluster n ($\delta_n>0$). The four possible displacements of the P atom in the $n=1$ and 3 clusters are therefore

$$\Delta\mathbf{r}_1(n)=\frac{\delta_n}{\sqrt{3}}(1,1,1)\ ,$$
$$\Delta\mathbf{r}_2(n)=\frac{\delta_n}{\sqrt{3}}(-1,-1,1)\ ,$$
$$\Delta\mathbf{r}_3(n)=\frac{\delta_n}{\sqrt{3}}(1,-1,-1)\ , \tag{C1}$$
$$\Delta\mathbf{r}_4(n)=\frac{\delta_n}{\sqrt{3}}(-1,1,-1)\ ,$$

and the probabilities of the four displacements are equal to

$$P[\Delta\mathbf{r}_i(n=1,3)]=P^{(n=1,3)}(x)/4\ , \tag{C2}$$

where $P^{(n)}(x)$ is given in Eq. (B2).

(iii) In the $n=2$ cluster there are two long In-P bonds and two short Ga-P bonds, so the P atom is displaced along one of the six (100), $(\bar{1}00)$, (010), $(0\bar{1}0)$, (001), or $(00\bar{1})$ directions (the middle of the two bonds). Let ε be the amplitude of the P-atom displacement along the (100) direction. The three possible displacements of the P atom in the $n=2$ cluster are

$$\Delta\mathbf{r}_1(n=2)=\varepsilon(1,0,0)\ ,$$
$$\Delta\mathbf{r}_2(n=2)=\varepsilon(0,1,0)\ , \tag{C3}$$
$$\Delta\mathbf{r}_3(n=2)=\varepsilon(0,0,1)\ ,$$

where $\varepsilon>0$, and $\Delta\mathbf{r}_4$, $\Delta\mathbf{r}_5$, and $\Delta\mathbf{r}_6$ are similar terms but with $\varepsilon<0$. The probabilities of the six displacements are equal to

$$P[\Delta\mathbf{r}_i(n=2)]=P^{(n=2)}(x)/6\ . \tag{C4}$$

For simplicity we choose

$$\delta_1(x)=-\delta_3(x)=\tfrac{1}{2}[\langle R_{In\text{-}P}(x)\rangle-\langle R_{Ga\text{-}P}(x)\rangle]\ , \tag{C5}$$

where $\langle R_{In\text{-}P}(x)\rangle$ and $\langle R_{Ga\text{-}P}(x)\rangle$ are the In-P and Ga-P average bond lengths in the random alloy. It is easy to see from the geometry of the cluster that

$$\varepsilon(x)=\cos\left[\frac{\theta}{2}\right][\langle R_{In\text{-}P}(x)\rangle-\langle R_{Ga\text{-}P}(x)\rangle]\ , \tag{C6}$$

where θ is the tetrahedral bond angle [$\theta=109.47°$, $\cos(\theta/2)=1/\sqrt{3}$]. Figure 12 demonstrates the possible displacements of the P atom. Thus in a three-dimensional representation of P-atom displacements there are 15 possible locations for the P atom. These are related to the five different nearest-neighbor local clusters $Ga_{4-n}In_n$ around the P atom: One undisplaced location is in the center of the $n=0$ and 4 tetrahedra, four displaced locations are in the (111), $(\bar{1}\,\bar{1}1)$, $(1\bar{1}\,\bar{1})$, or $(\bar{1}1\bar{1})$ directions of the $n=1$ clusters; four locations in $n=3$ are opposite to those of the $n=1$ clusters; and six displaced locations are in the (100), $(\bar{1}00)$, (010), $(0\bar{1}0)$, (001), and $(00\bar{1})$ directions of the $n=2$ clusters. These locations are represented in Fig. 11 by the three projected (100), (110), and (111) planes.

In order to make the model more realistic and closer to the statistical results, we broaden the projected displacements $\Delta\mathbf{r}_i(n)$ by a symmetric Gaussian

$$G(\Delta x,\Delta y)=e^{-(\Delta x^2+\Delta y^2)/2\sigma^2}\ , \tag{C7}$$

where σ was chosen arbitrarily to be equal for all displacements. The results of the model are shown on the right-hand panels of Fig. 11. We see that the model qualitatively matches the results of the numerical simulation. We conclude therefore that, at $T=0$, the equilibrium locations of the P atoms in the random $Ga_{1-x}In_xP$ alloy are affected mainly by the nearest-neighbor environment.

[1]J. C. Woolley, in *Compound Semiconductors,* edited by R. K. Willardson and H. L. Goering (Reinhold, New York, 1962), p. 3.
[2]M. Jaros, Rep. Prog. Phys. **48**, 1091 (1985).
[3]O. Madelung, M. Schulz, and H. Weiss, in *Physics of III-V Compounds,* edited by O. Madelung, Landolt-Bornstein, New Series, Group III, Vol. 17, Pt. a (Springer-Verlag, Berlin, 1982).
[4]J. E. Bernard and A. Zunger, Phys. Rev. B **34**, 5992 (1986).
[5]J. E. Bernard and A. Zunger, Phys. Rev. B **36**, 3196 (1987).
[6]L. G. Ferreira, S.-H. Wei, and A. Zunger, Phys. Rev. B **40**, 3197 (1989).
[7]The experimental and theoretical results for spontaneous ordering in semiconductors alloys were recently reviewed by A. Zunger and S. Mahajan, in *Handbook of Semiconductors,* 2nd ed., edited by S. Mahajan (Elsevier, Amsterdam, 1994), Vol. 3B, p. 1399.
[8]F. Glas, C. Gors, and P. Henoc, Philos. Mag. B **62**, 373 (1990).
[9]A. L. Efros and M. E. Raikh, in *Optical Properties of Mixed Crystals,* edited by R. J. Elliot and I. P. Ipatorie, Modern Problems in Condensed Matter Science Vol. 23 (Elsevier, Amsterdam, 1988), p. 133.
[10]G. Landa, Solid State Commun. **86**, 351 (1993).
[11]J. B. Boyce and J. C. Mikkelsen, Jr., J. Cryst. Growth **98**, 37 (1989).
[12]S. M. Islam and B. A. Bunker, Physica B **158**, 606 (1989).
[13]A. Balzarotti, N. Motta, A. Kisiel, M. Zimnal-Starnawska, M. T. Czyzyk, and M. Podgorny, Phys. Rev. B **31**, 7526 (1985); N. Motta, A. Balzarotti, P. Letardi, A. Kisiel, M. T. Czyzyk, M. Zimmal-Starnawska, and M. Podgorny, Solid State Commun. **53**, 509 (1985); A. Balzarotti, M. T. Czyzyk, A. Kisiel, N. Motta, M. Podgorny, and M. Zimnal-Starnawska, Phys. Rev. B **30**, 2295 (1983).
[14]J. L. Martins and A. Zunger, Phys. Rev. B **30**, 6217 (1984).
[15]C.-Y. Yeh, A.-B. Chen, and A. Sher, Phys. Rev. B **43**, 9138 (1991).
[16]Y. Cai and M. F. Thorpe, Phys. Rev. B **46**, 15 879 (1992).
[17]M. Podgorny, M. T. Czyzyk, A. Balzarotti, P. Letardi, N. Motta, A. Kisiel, and M. Zimnal-Starnawska, Solid State Commun. **55**, 413 (1985).
[18]J. A. Barker, Proc. R. Soc. London **216**, 45 (1953).
[19]F. Schmid and K. Binder (unpublished).
[20]D. de Fontaine, in *Solid State Physics,* edited by H. Ehrenreich, F. Seitz, and D. Turnbull (Academic, New York, 1979), Vol. 34, p. 73.
[21]K. Binder, in *Festkörperprobleme (Advences in Solid State Physics),* edited by P. Grosse (Vieweg, Braunschweig, 1986), Vol. 26, p. 133.
[22]B. Dünweg and D. P. Landau, Phys. Rev. B **48**, 14 182 (1993).
[23]P. C. Kelires and J. Tersoff, Phys. Rev. Lett. **63**, 1164 (1989).
[24]D. P. Landau, in *Monte Carlo Methods in Statistical Physics,* edited by K. Binder (Springer-Verlag, Berlin, 1979), pp. 121–143.
[25]N. Metropolis, A. W. Rosenbluth, M. N. Rosenbluth, A. H. Teller, and E. Teller, J. Chem. Phys. **21**, 1087 (1953).
[26]R. Kikuchi, J. Chem. Phys. **60**, 1071 (1974).
[27]A. Zunger, in *Nato Advanced Study Institute on Statics and Dynamics in Alloys,* edited by A. Gonis and P. Turchi (Plenum, New York, 1994), p. 361.
[28]H. Y. Wang, R. Najafabadi, D. J. Srolovitz, and R. LeSar, Phys. Rev. B **45**, 12 028 (1992).
[29]J. M. Rickman, R. Najafabadi, L. Zhao, and D. J. Srolovitz, J. Phys. C **4**, 4923 (1992).
[30]R. Najafabadi, H. Y. Wang, D. J. Srolovitz, and R. LeSar, Acta Metall. Mater. **39**, 3071 (1991).
[31]B. Chakraborty and Z. Xi, Phys. Rev. Lett. **68**, 2039 (1992).
[32]S. M. Foiles, Phys. Rev. B **32**, 7685 (1985).
[33]Z. W. Lu, S.-H. Wei, and A. Zunger, Phys. Rev. B **44**, 512 (1991).
[34]D. B. Laks, L. G. Ferreira, S. Froyen, and A. Zunger, Phys. Rev. B **46**, 12 587 (1992).
[35]S. de Gironcoli, P., Giannozzi, and S. Baroni, Phys. Rev. Lett. **66**, 2116 (1991).
[36]M. R. Weidmann and K. E. Newman, Phys. Rev. B **45**, 8388 (1992).
[37]F. Glas, J. Appl. Phys. **66**, 1667 (1989).
[38]K. A. Bertness, S. R. Kurtz, D. J. Friedman, A. E. Kibbles, C. Kramer, and J. Olson, Appl. Phys. Lett. **65**, 989 (1994).
[39]H. Fujii, Y. Ueno, A. Gomyo, K. Endo, and T. Suzuki, Appl. Phys. Lett. **61**, 737 (1992).
[40]W. T. Masselink and M. Zachau, J. Cryst. Growth **127**, 14 (1993).
[41]S. Fujita, T. Noda, A. Wagai, C. Nozaki, and Y. Ashizawa (unpublished).
[42]M. B. Panish and M. Ilegems, Proc. Solid State Chem. **7**, 39 (1972).
[43]G. B. Stringfellow, J. Cryst. Growth **27**, 21 (1974); **58**, 194 (1982).
[44]K. Ishida, T. Nomura, H. Tokunaga, H. Ohtani, and T. Nishizawa, J. Less-Common Metals **155**, 193 (1989).
[45]J. E. Bernard, R. G. Dandrea, L. G. Ferreira, S. Froyen, S.-H. Wei, and A. Zunger, Appl. Phys. Lett. **56**, 731 (1990).
[46]R. G. Dandrea, J. E. Bernard, S.-H. Wei, and A. Zunger, Phys. Rev. Lett. **64**, 36 (1990).
[47]C. K. Shin, W. E. Spicer, W. A. Harrison, and A. Sher, Phys. Rev. B **31**, 1139 (1985).
[48]A.-B. Chen and A. Sher, Phys. Rev. B **32**, 3695 (1985).
[49]K. E. Khor, T. Ito, and S. Das Sarma, J. Vac. Sci. Technol. B **8**, 669 (1990).
[50]S. Das Sarma and K. E. Khor, Appl. Surf. Sci. **60/61**, 99 (1992).
[51]S.-H. Wei, L. G. Ferreira, and A. Zunger, Phys. Rev. B **41**, 8240 (1990).
[52]P. N. Keating, Phys. Rev. **145**, 637 (1966).
[53]R. M. Martin, Phys. Rev. B **1**, 4005 (1970).
[54]The cohesive energies were obtained by adding the heat of formation from D. D. Wagman, W. H. Evans, I. Halow, V. B. Parker, S. M. Bailey, and R. H. Shumm, *National Bureau of Standards Technical Note 270* (United States Government Printing Office, Washington, D.C. 176, 1968), and the heat of atomization of the elements from C. Kittel, *Introduction to Solid State Physics,* 3rd. ed. (Wiley, New York, 1967), p. 98. These values are quoted in W. A. Harrison, *Electronic Structure and the Properties of Solids* (Freeman, New York, 1980), p. 176.
[55]Z. W. Lu, D. B. Laks, S.-H. Wei, and A. Zunger, Phys. Rev. B **50**, 6642 (1994).
[56]R. Magri, J. E. Bernard, and A. Zunger, Phys. Rev. B **43**, 1593 (1991).
[57]S.-H. Wei and H. Krakauer, Phys. Rev. Lett. **55**, 1200 (1985).
[58]S. Kirkpatrick, C. D. Gelatt, Jr., and M. P. Vecchi, Science **220**, 671 (1983); A. Silverman and J. Adler, Comput. Phys. **6**, 277 (1992).
[59]K. E. Khor and S. Das Sarma, J. Vac. Sci. Technol. B **10**, 1994 (1992).
[60]We thank Dr. K. E. Khor for making this suggestion to us.
[61]L. M. Foster and J. F. Woods, J. Electrochem. Soc. **118**, 1175 (1971).

[62]R. F. Brebrick and R. J. Panlener, J. Electrochem. Soc. **121**, 932 (1974).

[63]V. T. Bublik and V. N. Leikin, Phys. Status Solidi A **46**, 365 (1978).

[64]For the common tangent method to calculate the phase diagram see, for example, C. H. P. Lupis, *Chemical Thermodynamics of Materials* (North-Holland, Amsterdam, 1983), p. 67.

[65]T. Mokri, K. Nakamura, and T. Ito, J. Appl. Phys. **70**, 1320 (1991).

[66]K. Nakamura and T. Mokri, Modeling Simul. Mater. Sci. Eng. **1**, 143 (1993).

[67]K. Onabe, Jpn. J. Appl. Phys. **21**, L323 (1982).

[68]N. Marzari, S. de Gironcoli, and S. Baroni, Phys. Rev. Lett. **72**, 4001 (1994).

[69]F. Glas, in *Proceedings of the Conference on Microscopic Semiconducting Materials,* IOP Conf. Proc. No. 134 (Institute of Physics and Physical Society, London, 1993), p. 269.

[70]P. Henoc, A. Izrael, M. Quillec, and H. Launois, Appl. Phys. Lett. **40**, 963 (1982); A. G. Norman, and G. R. Booker, J. Appl. Phys. **57**, 4715 (1985); Inst. Phys. Conf. Ser. **76**, 257 (1984).

[71]C. W. Gear, *Numerical Initial-Value Problems in Ordinary Differential Equations* (Prentice-Hall, Englewood Cliffs, NJ 1971), p. 49.

[72]G. D. Garbulsky and G. Ceder, Phys. Rev. B **49**, 6327 (1994).

[73]See data collected in D. N. Talwar and B. K. Agrawal, J. Phys. C **7**, 2981 (1974), and references therein; E. F. Skelton, P. L. Radoff, P. Bolsaitis, and A. Verbalis, Phys. Rev. B **5**, 3008 (1972); A. A. Vaipolin, Fiz. Tverd. Tela (Leningrad) **15**, 1223 (1973) [Sov. Phys. Solid State **15**, 825 (1973)]; J. Bashir, N. M. Butt, and Q. H. Khan, Acta Crystallogr. Sec. A **44**, 638 (1988); C. S. Guenzer and A. Bienestock, Phys. Rev. B **8**, 4665 (1973); T. Yamanaka and M. Tokonami, Acta Crystallogr. Sec. B **41**, 298 (1985); R. D. Horning and J. L. Staudenmann, Phys. Rev. B **34**, 3970 (1986); J. L. Baudour, M. M. Granger, L. Touper, R. Granger, and R. Triboulet, J. Phys. Chem. Solids **50**, 309 (1989); N. N. Sirota and V. D. Yanovich, in *Chemical Bonds in Semiconductors and Thermodynamics,* edited by N. N. Sirota (Consultants Bureau, New York, 1967), p. 144; M. J. Cooper, K. D. Rouse, and H. Fuess, Acta Crystallogr. Sec. A **29**, 49 (1973).

[74]R. Curles, G. Landa, and J. B. Renucci, Solid State Commun. **53**, 179 (1985); **86**, 351 (1993).

[75]D. Comedi, R. Kalish, and V. Richter, Phys. Rev. Lett. **61**, 2125 (1988).

[76]T. Haga, T. Kimura, Y. Abe, T. Fukui, and H. Saito, Appl. Phys. Lett. **47**, 1162 (1985).

[77]D. Comedi and R. Kalish, Phys. Rev. B **46**, 15 844 (1992).

[78]We got the following rms displacements for the binaries ZnTe and CdTe: $U_{Zn}(ZnTe)=0.071$ Å, $U_{Te}(ZnTe)=0.060$ Å, $U_{Te}(CdTe)=0.065$ Å, and $U_{Cd}(CdTe)=0.080$ Å compared to the experimental results of Comedi and Kalish [$U_{Zn}(ZnTe)=0.125\pm0.01$ Å, $U_{Te}(ZnTe)=0.095\pm0.01$ Å, $U_{Te}(CdTe)=0.135\pm0.01$ Å, and $U_{Cd}(CdTe)=0.155\pm0.01$ Å]. We observe that although there is a factor of about 2 between these experimental results and ours, the trend in the relations between the anions and cations is reproduced.

[79]L. Reinhard and S. C. Moss (unpublished); U. Gahn and W. Pitsch, Z. Metall. **78**, 324 (1987).

[80]L. C. Feldman, J. W. Hayer, and S. T. Picraux, *Material Analysis by Ion Channeling* (Academic, New York, 1982).

[81]D. Comedi, R. Kalish, and J. H. Barrett, Nucl. Instrum. Methods Phys. Res. Sect. B **63**, 451 (1992).

[82]A. Baldereschi and M. Peressi, J. Phys. Condens. Matter **5**, B37 (1993).